This article has been accepted for publication in a future issue of this journal, but has not been fully edited. Content may change prior to final publication. Citation information: DOI 10.1109/TGRS.2022.3143167, IEEE Transactions on Geoscience and Remote Sensing

A daytime multi-sensor satellite system for global gas flaring monitoring

Mariapia Faruolo, Alfredo Falconieri, Nicola Genzano, Teodosio Lacava, Francesco Marchese, and Nicola Pergola

***Abstract*—Natural gas flaring (GF) is a longstanding problem for the oil industry. Recent estimates indicate that this phenomenon has increased to levels recorded a full decade earlier. While in 2020 there was a decline in global GF due to COVID-19 pandemic, data suggest that GF continues to be a persistent issue, with solutions remaining difficult or uneconomical in certain countries. Nighttime satellite products are widely used to map and monitor GF affected areas, partially filling the general lack of information from oil companies and/or national reporting. In this work, we assess the potential of daytime infrared satellite observations at high spatial resolution from Operational Land Imager (OLI) and Multispectral Instrument (MSI) sensors, respectively onboard Landsat-8 (L8) and Sentinel-2 (S2) satellites, in monitoring GF activity. The Normalized Hotspot Indices (NHI) algorithm is used for this purpose, testing its performance over six different GF sites. Results show the NHI capability in providing accurate information about GF related thermal (e.g., 100% of detections offshore; up to 92% onshore), despite some limitations due to clouds and smoke. They open challenging scenarios regarding the possibility of quantifying the volume of emitted gas from daytime S2-MSI and L8-OLI data, integrating information from well-established nighttime operational systems.**

***Index Terms*— daytime gas flaring tracking, Normalized Hotspot Indices, OLI Landsat 8 and MSI Sentinel 2, shortwave and near infrared channels, thermal anomalies detection.**

I. INTRODUCTION

GAS flaring represents a longstanding problem for the oil industry [1]. It is globally recognized as a contributor to global warming and climate changes, and as a waste of clean energy [2],[3]. Despite the rising awareness of the problem, and a number of initiatives, which aim to curb flaring [4], continued misuse of a large proportion of the associated gas is being recorded, at global scale, by satellite data and insights provided by the U.S. National Oceanic and Atmospheric Administration (NOAA) [5]. Of an estimated 935 Billion Cubic Meters (BCM) of gas, extracted in association with oil in 2019, only about 75% ended up being used on-site by the operator, or reinjected into the well, or marketed to consumers. Of the remaining 25%, about 55 BCM was released as methane into the atmosphere, and the remaining 150 BCM flared.5 While 2020 saw a 10% decline in global gas flaring [6], owing to COVID-19 pandemic, data suggest that gas flaring continues to be a persistent problem, with solutions remaining difficult or uneconomical in certain countries [5]. Beyond the complex problems related to the flaring of natural gas (e.g., poor planning, lack of infrastructure or incentives), the main challenge is to quantify this phenomenon and its effects on the environment [7],[8]. Indeed, only a few countries systematically measure, record and release flaring data publicly. The lack of information from the oil companies and/or national reporting does not enable an accurate assessment of the amount of emitted gas. On the other hand, information about flaring of natural gas is mostly derived from satellite observations [1]. Since about two decades, under the pressure of the World Bank and Global Gas Flaring Reduction partnership cooperation, the Earth Observation Group (EOG) at the Colorado School of Mines publishes flaring data for approximately 85 countries, on an annual basis, through the analysis of multi-temporal and multi-platform satellite data [4]. To date, despite the considerable progress in this research field, satellite data/products can be profitably used to: i) identify flaring sites, ii) characterize thermal emissions; iii) estimate gas flaring emissions [9].

At the current state, gas flaring is analyzed through infrared (from near to thermal) satellite observations acquired in nighttime conditions from sensors such as the Visible Infrared Imaging Radiometer Suite (VIIRS) [10]-[12]. Nighttime satellite data are the most suited to detect and quantify gas flaring activity [13],[14]. This encouraged the development of several satellite-based methods, listed and detailed in [9], to detect gas flaring thermal anomalies and discriminate them from other hot targets. Indeed, since the solar reflectance represents a major issue, only a few studies [6],[10] assessed the possibility of using sensors such as Thematic Mapper (TM) and the Operational Land Imager (OLI) to investigate industrial gas flaring by satellite in daylight conditions [15],[16]. Those preliminary studies suggested the use of a multi-spectral approach to overcome the daytime detection drawbacks; nonetheless, this approach was not implemented so far.

In this study, we assess the potential of a recent multi-channel algorithm, developed to map volcanic thermal anomalies, and running operationally within the Google Earth Engine (GEE) environment [17], in providing information about gas flaring activity in daylight conditions. In detail, the Normalized Hotspot Indices (NHI) algorithm [18] is used for this purpose.

M. Faruolo, A. Falconieri, T. Lacava, F. Marchese and N. Pergola are with the Institute of Methodologies for Environmental Analysis, National Research Council, Tito Scalo, Italy (e-mails: mariapia.faruolo@imaa.cnr.it, alfredo.falconieri@imaa.cnr.it, teodosio.lacava@imaa.cnr.it, francesco.marchese@imaa.cnr.it, nicola.pergola@imaa.cnr.it).

N. Genzano is with the School of Engineering, University of Basilicata, Potenza, Italy (e-mail: nicogenzano@gmail.com).

0196-2892 (c) 2021 IEEE. Personal use is permitted, but republication/redistribution requires IEEE permission. See http://www.ieee.org/publications_standards/publications/rights/index.html for more information.
Authorized licensed use limited to: CNR Area Ricerca Potenza. Downloaded on February 03,2022 at 16:38:15 UTC from IEEE Xplore. Restrictions apply.

This article has been accepted for publication in a future issue of this journal, but has not been fully edited. Content may change prior to final publication. Citation information: DOI 10.1109/TGRS.2022.3143167, IEEE Transactions on Geoscience and Remote Sensing

Six flaring sites, characterized by different operational conditions, and flaring intensity, are investigated using OLI and, for the first time, MSI (Multispectral Instrument) data, at 30/20 m spatial resolution, respectively. In addition, we verify if NHI is capable of detecting gas flaring activity at global scale (i.e., over both onshore and offshore sites) also through satellite data at mid-low spatial resolution (e.g., VIIRS). The work aims to fill the current observational gaps in investigating gas flares from space, integrating information from the well-established VIIRS NightFire (VNF) algorithm, operating in nighttime [10],[11]. This integration represents a novelty in the framework of gas flaring monitoring. By improving the continuity and accuracy of observation, it may better address the growing of this relevant industrial phenomenon.

II. Test Sites

Fig. 1 shows the total amount of volumes of gas flared measured in BCM, whose values were downloaded from the EOG website (https://eogdata.mines.edu/download_global_flare.html), for each country hosting the gas flaring site analyzed in this study, over the period 2012-2019. Countries labeled in darkest pink are associated with the highest gas flaring volume.

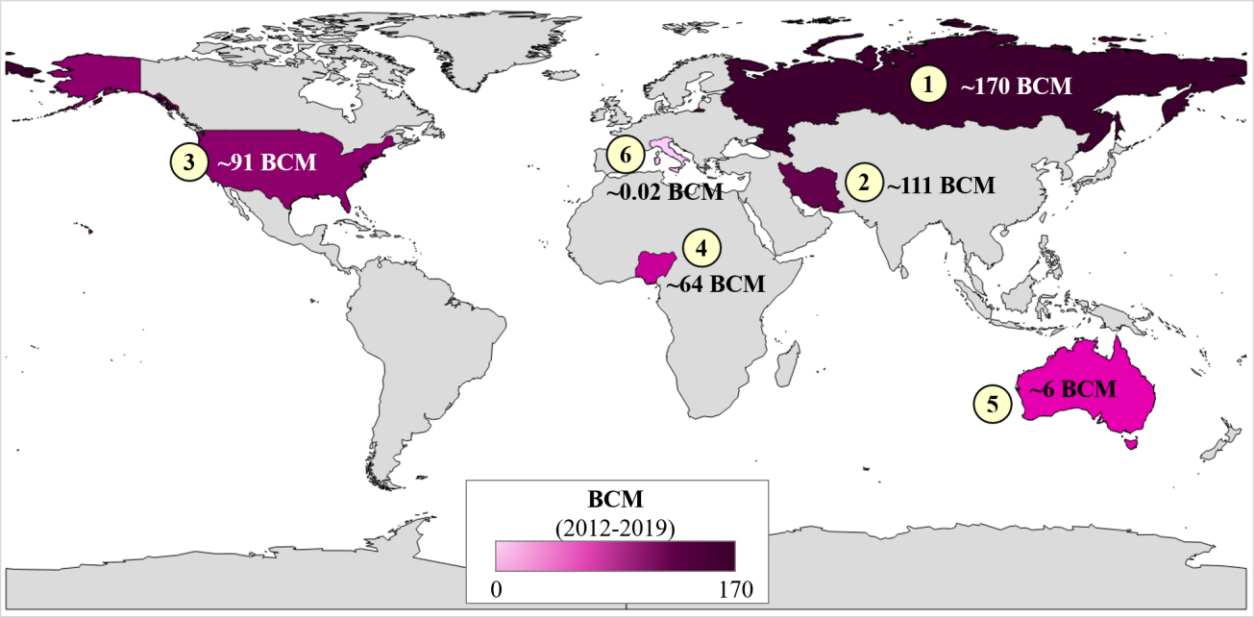

Fig. 1. Upstream gas flaring in BCM for the countries hosting the investigating test sites: (1) Russian Federation; (2) Iran; (3) United States; (4) Nigeria; (5) Australia; (6) Italy.

The most significant differences in the flaring intensity are driven by three factors, namely: (i) the intrinsic gassiness of the resource; (ii) the approach the operator takes to use the produced gas; (iii) the "waste disposal" method [1]. Those factors strongly affect the thermal behavior of the source. Moreover, since gas flaring can be a continuous or a temporary practice [9], the related thermal anomaly could be not persistent in time.

The Russian Federation, United States and Iran have been among the countries responsible for more than half of global gas flaring, over the period 2017-2019 [19],[20]. Notably, the increase of BCM recorded 2019 is primarily due to United States (up 23%) and Russia (up 9%), which account for about 40% of global oil production) [21]. Nigeria successfully reduced flaring by 70% in between 2000 and 2019. However, gas flaring activity is still relevant; Nigeria's Department of Petroleum Resources initiated a conference to tackle existing gas flaring at 45 sites [19]. Australia and Italy flare a fewer amount of gas (less than 0.006 and 0.001 BCM each year, respectively) than the other countries (1-2 orders of magnitude lower). In Australia, flaring intensity is not decreasing in time. The negligible values recorded in Italy are related to the significant investments of oil companies in recovering the associated gas.

Fig. 2A displays the BCM flared by each plant during 2012-2020 (the darker green the higher the BCM). The gas flaring sites analyzed here are located in the Volgograd Oblast region (Russian Federation, Fig. 2B), North Dakota (United States, Fig. 2C), Bayelsa region (Nigeria, Fig. 2D), New South Wales (Australia, Fig. 2E) and Basilicata region (Italy, Fig. 2F). The only gas flare located offshore is in the Persian Gulf (Iran, Fig. 2G). Fig. 2B-G then shows the plant system and the histogram of source temperature provided by the EOG team starting from VNF detections [10],[11], over the period 2012-2020.

0196-2892 (c) 2021 IEEE. Personal use is permitted, but republication/redistribution requires IEEE permission. See http://www.ieee.org/publications_standards/publications/rights/index.html for more information.
Authorized licensed use limited to: CNR Area Ricerca Potenza. Downloaded on February 03,2022 at 16:38:15 UTC from IEEE Xplore. Restrictions apply.

This article has been accepted for publication in a future issue of this journal, but has not been fully edited. Content may change prior to final publication. Citation information: DOI 10.1109/TGRS.2022.3143167, IEEE Transactions on Geoscience and Remote Sensing

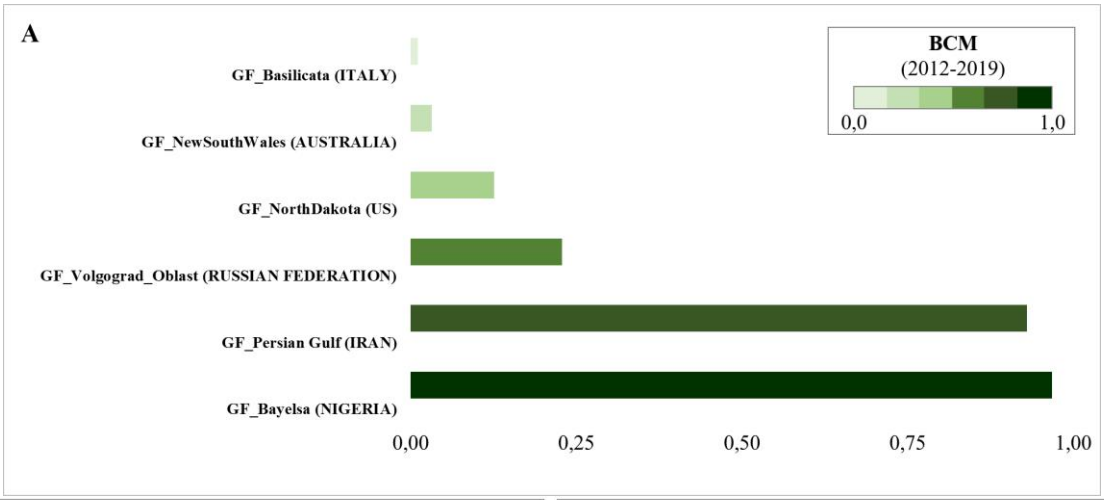

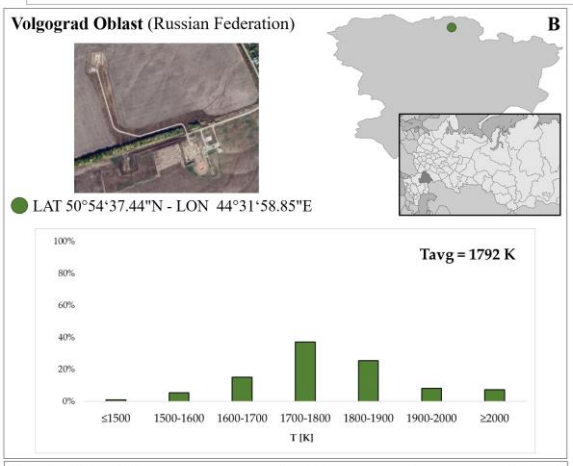

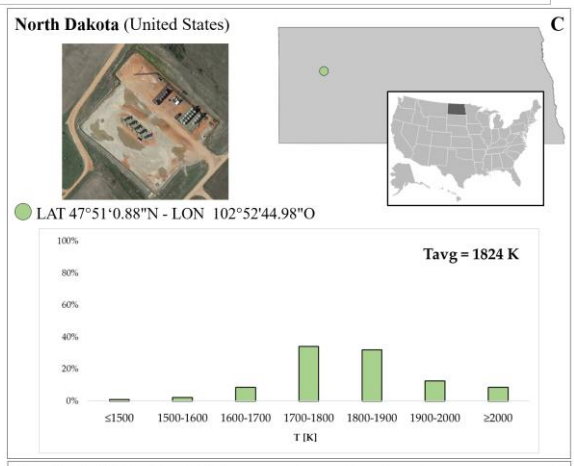

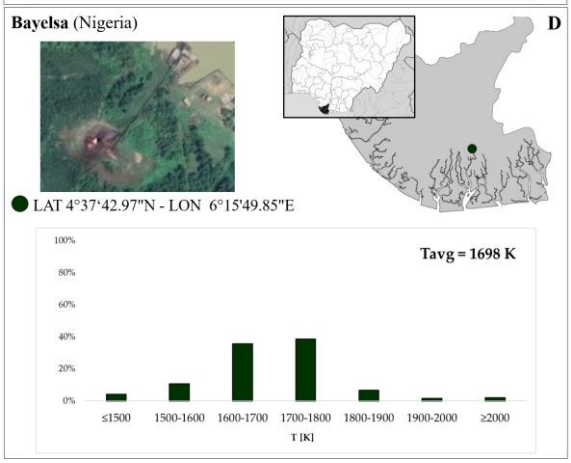

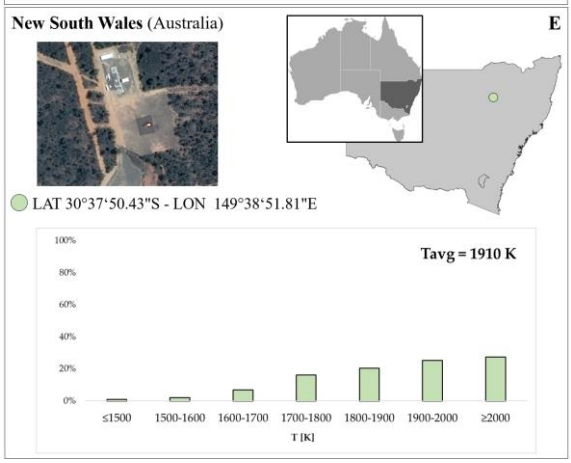

0196-2892 (c) 2021 IEEE. Personal use is permitted, but republication/redistribution requires IEEE permission. See http://www.ieee.org/publications_standards/publications/rights/index.html for more information.
Authorized licensed use limited to: CNR Area Ricerca Potenza. Downloaded on February 03,2022 at 16:38:15 UTC from IEEE Xplore. Restrictions apply.

This article has been accepted for publication in a future issue of this journal, but has not been fully edited. Content may change prior to final publication. Citation information: DOI 10.1109/TGRS.2022.3143167, IEEE Transactions on Geoscience and Remote Sensing

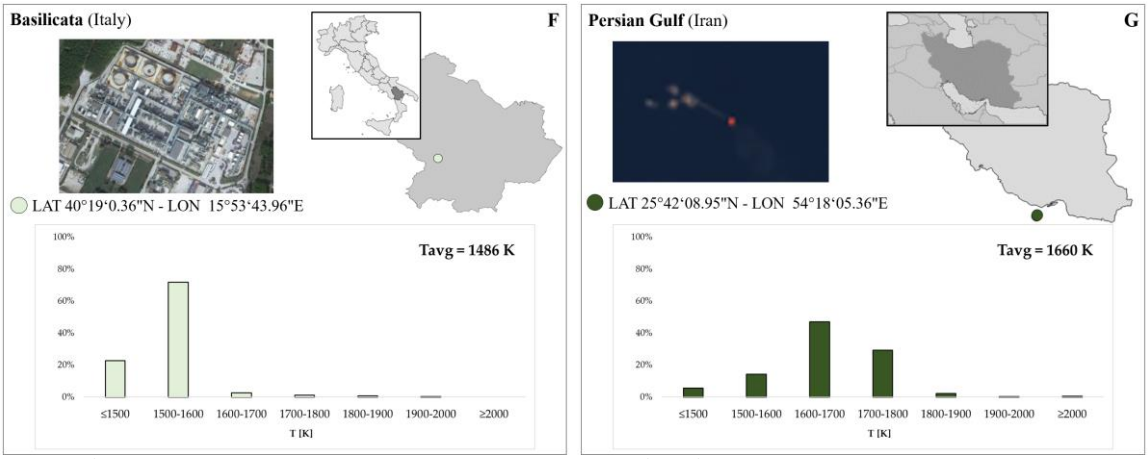

Fig 2. A) Total BCM flared by each investigated site in years 2012-2019. Features of gas flares investigated in this work, located in B) Russian Federation (Volgograd Oblast), C) United States (North Dakota), D) Nigeria (Bayelsa region), E) Australia (New South Wales), F) Italy (Basilicata region), G) Persian Gulf (Iran; in background the S2A-MSI true color composite, B4: 0.664 μm, B3: 0.559 μm, B2: 0.492 μm, of January 12, 2018 at 07:09 UTC). For each site, a picture showing the plant (taken from Google Earth) and a graph with its temperature range distribution are reported.

Test sites exhibit an average temperature above 1450 K, which is typical of gas flares [9]. Among them, only the Basilicata one is usually operating at temperatures below 1600 K, confirming its hybrid behavior in terms of source temperature, as already shown in a previous paper [22]. Fig. 2F shows that it is a complex plant, where flares operate jointly with the baseload gas recovery systems, reducing the process flaring significantly [22],[23]. All the other sites analyzed here have temperatures above 1600 K (with peaks up to 2000 K), showing a more intense gas flaring activity.

III. The Normalized Hotspot Indices Algorithm

Hot sources at flaring temperatures emit most thermal radiation in the IR region of the electromagnetic spectrum. The peak of thermal emissions shifts from Medium Infrared (MIR) (3-3.5 μm for a hot source at 800-1000 K) to Shortwave Infrared (SWIR) region, at the increasing temperatures (e.g., 2.2 μm at ~1400 K, 1.6 μm at ~1800 K). The thermal signature (i.e., intensity, spatial distribution and temporal persistency) of thermal anomalies associated with industrial gas flaring activity may then vary in both space and time, based on conditions at which the plant manages the natural gas, and on temporal continuity of the practice (continuous, periodic or sporadic). A detailed explanation of gas flares spectral behavior can be found in [9].

The NHI algorithm analyzes the radiances measured in the Near Infrared (NIR) and SWIR bands of OLI and MSI sensors, respectively onboard Landsat-8 (L8) and Sentinel-2 (S2) satellites, to detect thermal anomalies in daytime conditions, through the computation of two normalized indices:

$$NHI_{SWIR} = (L_{SWIR2} - L_{SWIR1})/(L_{SWIR2} + L_{SWIR1}) \quad (1)$$

$$NHI_{SWNIR} = (L_{SWIR1} - L_{NIR})/(L_{SWIR1} + L_{NIR}) \quad (2)$$

where L_{SWIR2}, L_{SWIR1}, L_{NIR} are the TOA (Top of Atmosphere) radiances (W m^{-2} sr^{-1} μm^{-1}) measured, for each pixel of the scene, at 2.2, 1.6 and 0.8 μm wavelengths, in the relative MSI/OLI spectral channels. Pixels showing positive values of one or both indices are flagged as "hot" by NHI [18]. Performance and limitations of this algorithm, which was developed to map volcanic thermal anomalies such as lava flows, at global scale, were widely described in previous papers, using data also from other sensors, such as the Advanced Spaceborne Thermal Emission and Reflection Radiometer [17],[26]-[27]. Moreover, NHI may be used to map also other hot targets such as gas flaring sources, which occupy a very low fraction of the pixel area (up to a few square meters) [12],[26], reaching temperatures in between 1600-2200 K [27].

Here, we investigate the NHI algorithm potential in analyzing the gas flaring at the sites of interest over the period 2015-2020. We used two versions of the algorithm for this purpose: the original configuration for the onshore, the version running operationally within the Google Earth Engine (GEE) App (https://sites.google.com/view/nhi-tool) for the offshore. The latter includes some spectral tests to detect extremely hot pixels (i.e., pixels showing saturation in OLI/MSI SWIR bands), and minimize the effects of multispectral misregistration of S2-MSI imagery [17], which may lead to false positives particularly over maritime platforms. Moreover, the NHI was for the first time implemented here also on Sea and Land Surface Temperature Radiometer (SLSTR) and VIIRS data (both onshore and offshore).

IV. Data

OLI is one of the two instruments onboard the Landsat 8 satellite. The latter orbits the Earth in a sun-synchronous near-polar orbit, at an altitude of 705 km, with a 16 days repeat cycle (equatorial crossing time at 10:00 AM ± 15 min) [28]. OLI provides data in nine spectral bands from Visible (VIS) to SWIR region, with a spatial resolution of 15 m (panchromatic) and 30 m (VNIR/SWIR bands). L8-OLI data, covering an area of 185 km ×180 km, are distributed by the United States Geological Survey (USGS) in Universal Transverse Mercator (UTM)/World Geodetic System (WGS) 1984 projection [29]. To run the NHI algorithm, we converted data from digital

0196-2892 (c) 2021 IEEE. Personal use is permitted, but republication/redistribution requires IEEE permission. See http://www.ieee.org/publications_standards/publications/rights/index.html for more information.
Authorized licensed use limited to: CNR Area Ricerca Potenza. Downloaded on February 03,2022 at 16:38:15 UTC from IEEE Xplore. Restrictions apply.

This article has been accepted for publication in a future issue of this journal, but has not been fully edited. Content may change prior to final publication. Citation information: DOI 10.1109/TGRS.2022.3143167, IEEE Transactions on Geoscience and Remote Sensing

numbers (DNs) to TOA radiance, using the rescaling coefficients available in the metadata (MTL) file.

The MSI sensor flies at a mean orbital altitude of 786 km onboard the Sentinel-2 constellation (Sentinel-2A/2B satellites), which guarantees a revisit time of 5 days, increasing up to 2-3 days at the mid-high latitude regions [30]. The MSI has a 290 km swath width (significantly larger than the OLI one) and a mean local time of 10:30 AM. The instrument provides data in 13 spectral bands (0.443–2.190 μm), with a spatial resolution of 10 m (VNIR), 20 m (VNIR vegetation red edge and SWIR) and 60 m (atmospheric correction bands). The NHI algorithm uses the Level-1C product (calibrated TOA reflectance), which is distributed through the Copernicus Open Access Hub (https://scihub.copernicus.eu/dhus/#/home). This product, composed of 100 km x 100 km tiles, in the UTM/WGS84 projection, contains ad-hoc parameters to transform reflectance into radiances [31],[32].

VIIRS, aboard Suomi National Polar-orbiting Partnership (NPP) and Joint Polar Satellite System-1 (JPSS-1) platforms, collects data in 22 spectral bands (0.412-12.01 μm). Infrared channels, at 375 m (Imagery bands) and 750 m (Moderate bands) spatial resolution, are commonly used to detect hotspots [33]. The VIIRS Sensor Data Record (SDR) used in this work, including both the Moderate (M07-M10-M11) and Imagery (I2-I3) bands (Table 1), were converted to radiance, and spatially clipped over the target areas, using the Polar2Grid v2.2 software (https://www.ssec.wisc.edu/software/polar2grid/).

The SLSTR, onboard Sentinel-3 satellite, acquires data from VIS to Thermal Infrared (TIR) region, with a spatial resolution ranging from 500 m (VIS-SWIR channels) to 1 km (TIR channels) at the nadir view. The high dynamic range of F2 (10.8 μm) and F1 (3.7μm) channels enables a more efficient identification and characterization of high-temperature features [34].

We used the spectral channels detailed in Table 1, in reference to the above-mentioned sensors, to detect thermal anomalies at flaring sites through the NHI algorithm in daylight conditions.

TABLE I
NIR AND SWIR CHANNELS OF OLI, MSI, VIIRS AND SLSTR SENSORS USED FOR THE COMPUTATION OF NHI INDICES (I = IMAGERY BANDS, M = MODERATE BANDS)

Sensor	Spectral Range (μm)		
	NIR	$SWIR_{1.6}$	$SWIR_{2.2}$
OLI	0.85 – 0.88 (B5)	1.57 – 1.65 (B6)	2.11 – 2.29 (B7)
MSI	0.845 – 0.885 (B8A)	1.52 – 1.70 (B11)	2.01 – 2.57 (B12)
VIIRS_I	0.846 – 0.885 (I2)	1.58 – 1.64 (I3)	
SLSTR	0.846 – 0.885 (M07)	1.58 – 1.64 (M10)	2.225 – 2.275 (M11)
VIIRS_M	0.85 – 0.89 (S3)	1.58 – 1.65 (S5)	2.23 – 2.28 (S6)

V. RESULTS

A. *Mapping the gas flaring sites*

In this section, we show the thermal anomaly maps at GF sites generated using the NHI algorithm under the GEE environment. The latter offers extended data archives of satellite observations and massive computational capabilities, which allow for geospatial analyses at planetary scale [22]. Thermal anomaly maps analyzed here display detected hot pixels in three different colors, providing qualitative information about intensity of gas flaring activity. Extremely hot pixels are depicted in violet, hot pixels (flagged by the NHI_{SWNIR} index) in red, and warm pixels (flagged by the NHI_{SWIR} index) in yellow. Here, we show some NHI detections performed over the gas flare areas of Volgograd Oblast (Fig. 3), Basilicata (Fig. 4), and Persian Gulf (Fig. 5). We performed the visual inspections of L8-OLI and S2-MSI scenes to assess the accuracy NHI detections. Moreover, we analyzed thermal anomaly maps also through comparison with a false composite color product used by USGS to emphasize hot targets. Table 2 details some satellite scenes, acquired under peculiar observational conditions, representative of the different gas flare sites analyzed in this study.

TABLE II
OLI AND MSI TILES DATA USED

Site Location	Tile ID		Acquisition Date		Acquisition Time (UTC)	
	OLI	MSI	OLI	MSI	OLI	MSI
Volgograd Oblast	172-24	T38UMB	February 7, 2017		07:53	08:15
Basilicata	188-32	T33TWE	December 14, 2019	February 14, 2017	09:35	09:45
Persian Gulf	161-42	T40RBP	December 8, 2016		06:52	07:02

The L8-OLI and S2-MSI tiles with gas flares were selected by querying the USGS Earth Explorer platform. Fig. 3-5 display the RGB (Red: SWIR1, Green: NIR, Blue: VIS) products, and the thermal anomaly maps showing hot pixels flagged by NHI overlapped to a static (for each site) very high-spatial resolution image available in GEE.

0196-2892 (c) 2021 IEEE. Personal use is permitted, but republication/redistribution requires IEEE permission. See http://www.ieee.org/publications_standards/publications/rights/index.html for more information.
Authorized licensed use limited to: CNR Area Ricerca Potenza. Downloaded on February 03,2022 at 16:38:15 UTC from IEEE Xplore. Restrictions apply.

This article has been accepted for publication in a future issue of this journal, but has not been fully edited. Content may change prior to final publication. Citation information: DOI 10.1109/TGRS.2022.3143167, IEEE Transactions on Geoscience and Remote Sensing

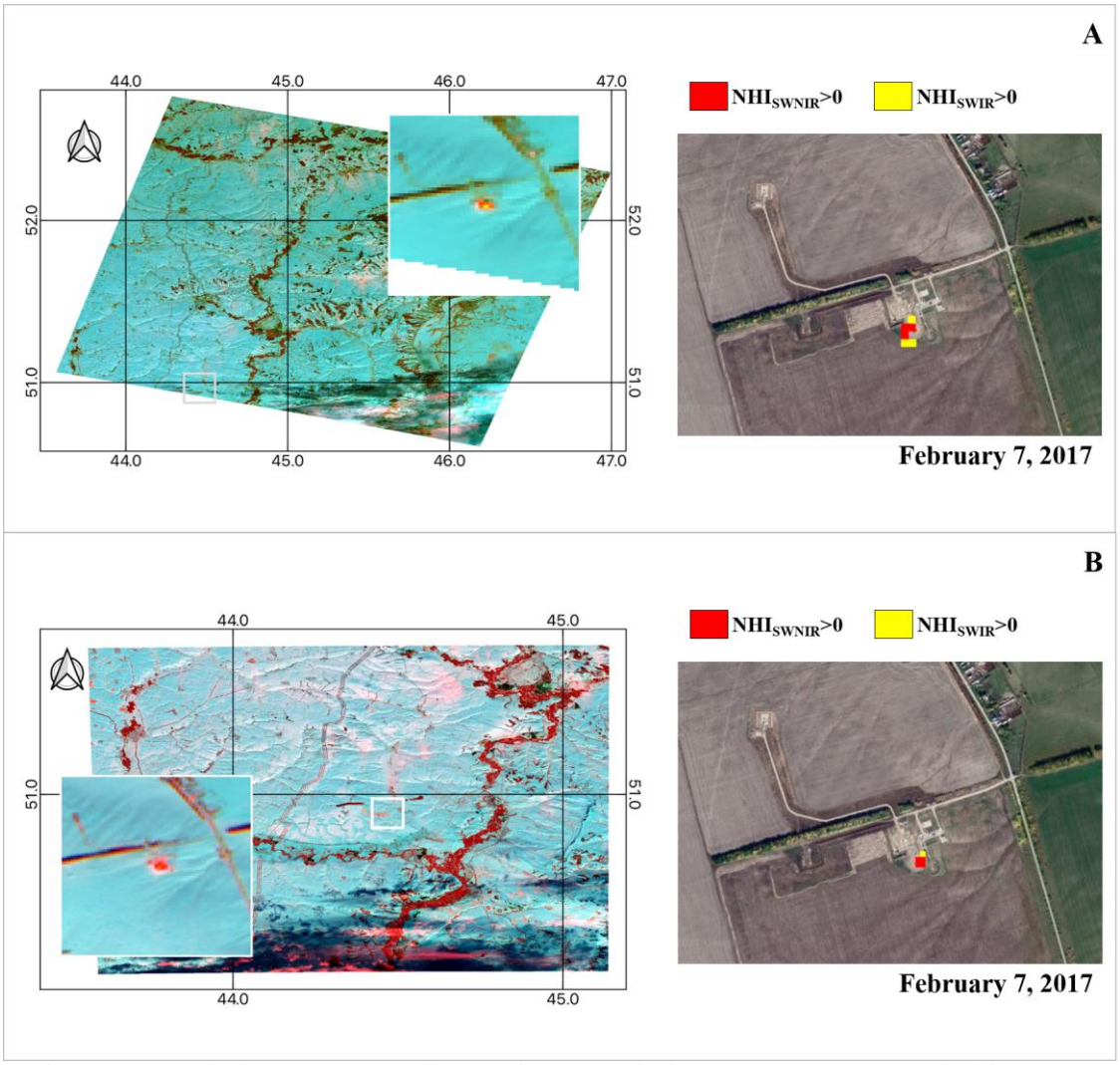

Fig 3. A) On the left, L8-OLI scene of February 07, 2017 (Credits: USGS/NASA's Earth Observatory), at 07:53 UTC; on the right, GEE-NHI detection (in red the NHI_{SWNIR}, in yellow the NHI_{SWIR}); B) As for (A) the S2A-MSI scene for the same day, at 08:15 UTC. The white box includes the Volgograd Oblast site. For each tile, the RGB in background.

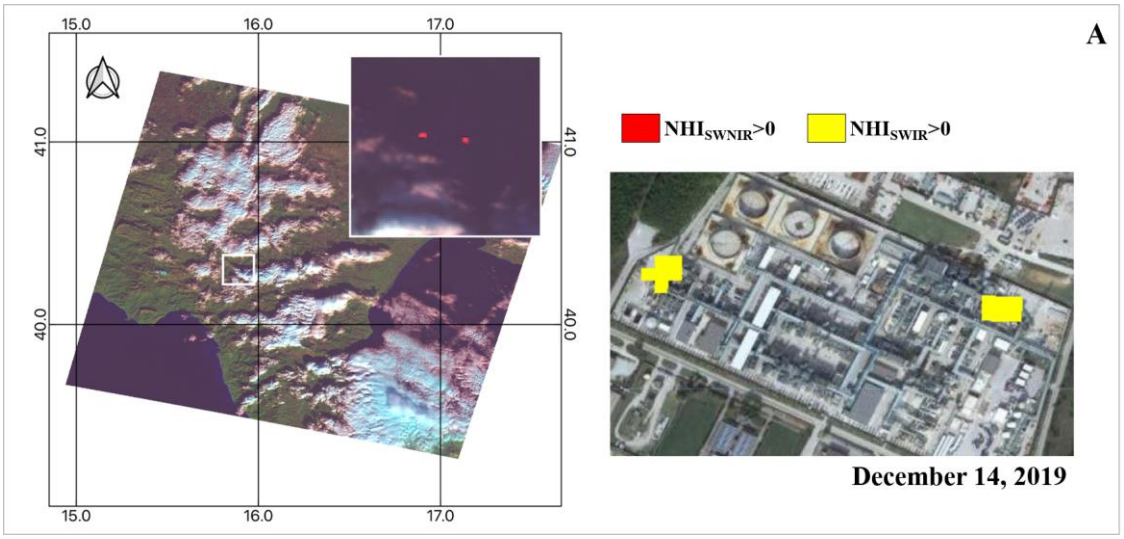

0196-2892 (c) 2021 IEEE. Personal use is permitted, but republication/redistribution requires IEEE permission. See http://www.ieee.org/publications_standards/publications/rights/index.html for more information.
Authorized licensed use limited to: CNR Area Ricerca Potenza. Downloaded on February 03,2022 at 16:38:15 UTC from IEEE Xplore. Restrictions apply.

This article has been accepted for publication in a future issue of this journal, but has not been fully edited. Content may change prior to final publication. Citation information: DOI 10.1109/TGRS.2022.3143167, IEEE Transactions on Geoscience and Remote Sensing

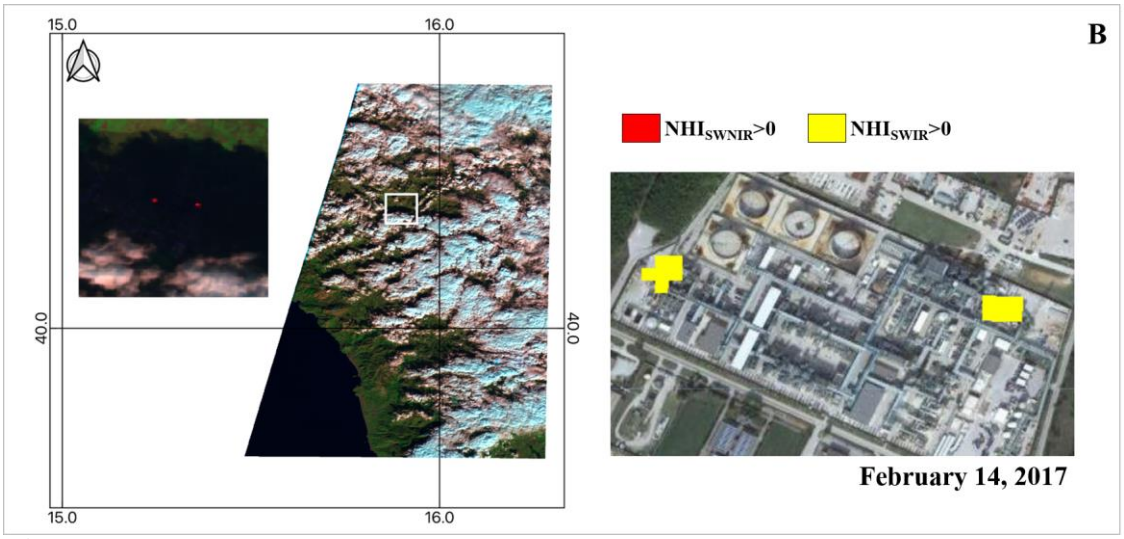

Fig 4. As Fig. 3, for the Basilicata site (highlighted in the white box) on A) December 14, 2019 by L8-OLI at 09:35 UTC and B) February 14, 2017 by S2A-MSI, at 09:45 UTC.

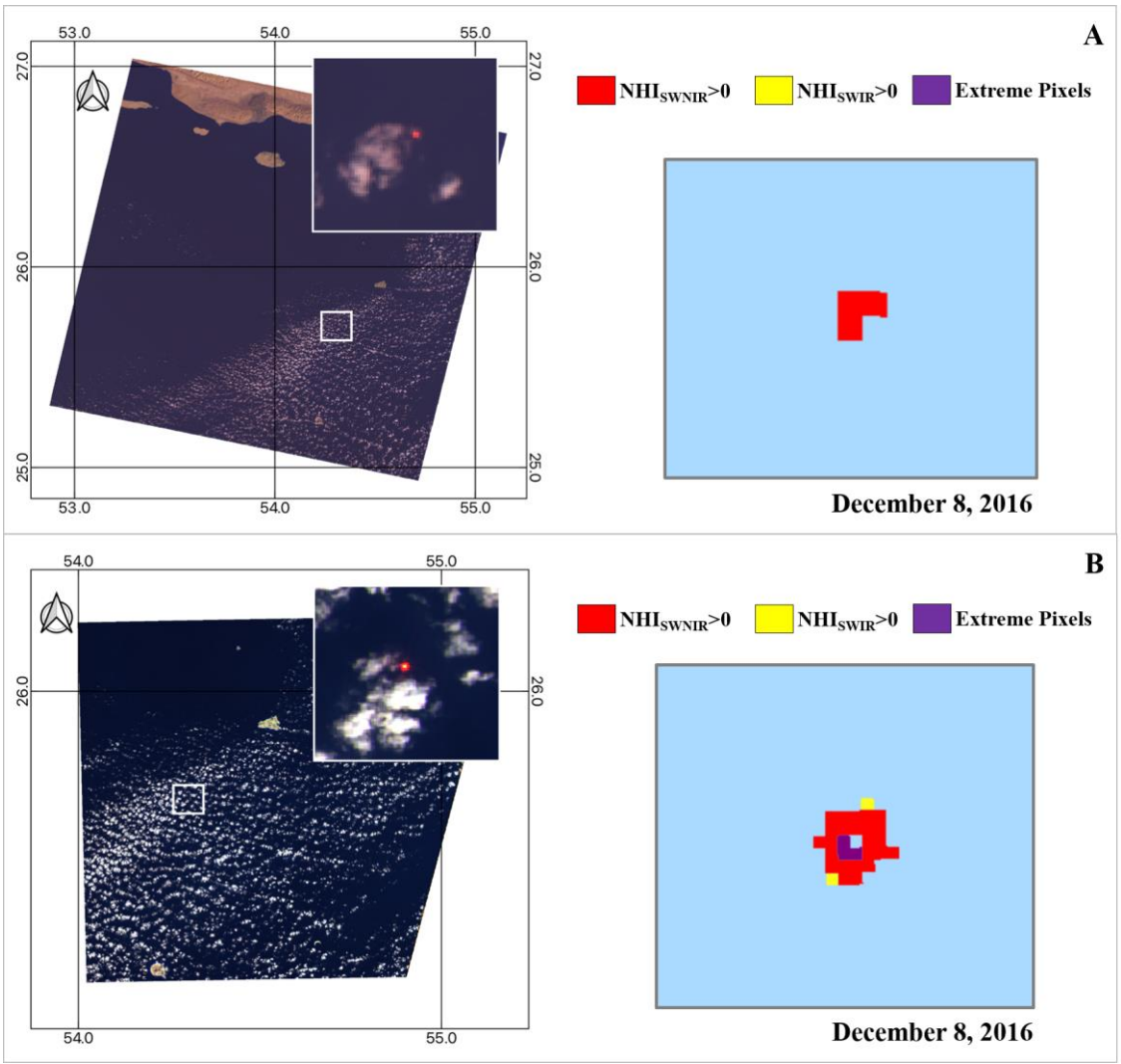

Fig 5. As Fig. 3, for the Persian Gulf site (highlighted in the white box) on December 8, 2016 by A) L8-OLI, at 06:52 UTC and B) S2A-MSI, at 07:02 UTC.

Map show that thermal anomalies flagged by NHI were consistent for both shape and spatial extent with information retrieved from the false color composite imagery (see pixels appearing red/yellow on left panels). The algorithm missed only a few hot pixels due to the presence of clouds/smoke (e.g., Fig. 5A). In spite of this limitation, mid-high spatial resolution satellite data enabled an efficient discrimination of gas flaring

0196-2892 (c) 2021 IEEE. Personal use is permitted, but republication/redistribution requires IEEE permission. See http://www.ieee.org/publications_standards/publications/rights/index.html for more information.
Authorized licensed use limited to: CNR Area Ricerca Potenza. Downloaded on February 03,2022 at 16:38:15 UTC from IEEE Xplore. Restrictions apply.

This article has been accepted for publication in a future issue of this journal, but has not been fully edited. Content may change prior to final publication. Citation information: DOI 10.1109/TGRS.2022.3143167, IEEE Transactions on Geoscience and Remote Sensing

sources as for Basilicata region, where two clusters of hot pixels were identified, in agreement with preliminary results of the gas flaring performed in [17]. These clusters exactly correspond to the areas reaching high temperatures during the crude oil pretreatment process, i.e., the flare plant (on the right) and the sulfur recovery system (on the left). Moreover, it is worth noting that as for Persian Gulf, NHI performed an efficient mapping of the areas where thermal emissions were particularly intense, i.e., in correspondence of the flare stack, or weaker (see yellow pixels at the borders of detected thermal anomaly). These results show that daytime S2-MSI and L8-OLI data may be used for an accurate localization and mapping of the gas flaring sources at global scale. Furthermore, it is worth pointing out that, in case of near-coincident acquisitions (less than 20 minutes apart), like the ones showed in Fig. 3 and Fig. 5, both the OLI and MSI instruments correctly detected flaring sites, i.e., showing positive values of the two NHI indices. According to this, it can be argued that the slight differences in spectral, spatial and temporal characteristics of the used satellite data do not have any significant impact on NHI capability in detecting GF sites, making the joint use of the two sensors a strength of the algorithm.

B. Investigation of detected thermal anomalies

Table 3 details the number of satellite scenes with thermal anomalies flagged by NHI at the investigated gas flares, over the period 2012-2020. The table includes, such as Fig. 6 showing the temporal trend of daily thermal anomalies, the extremely hot pixels associated with intense thermal emissions, yielding the saturation of SWIR channels (e.g., OLI B7 nominal saturation of 24.3 W m^{-2} sr^{-1} μm^{-1}) [36]-[38]. In Table 3, the third column (NHI > 0) wording means that the thermal anomaly was detected by at least one of the two normalized indices (i.e., "OR" condition), while the last column (NHI_{SWIR} > 0 AND NHI_{SWNIR} > 0) details the number of satellite scenes with positive values of both used indices. The total number of OLI and MSI data acquisitions, available for each analyzed gas flare site, is also reported (second column in Table 3).

TABLE III
NUMBER OF SATELLITE SCENES WITH NHI DETECTIONS IN REFERENCE TO THE SIX TEST SITES

Test Sites	# data	NHI > 0	NHI_{SWIR} > 0	NHI_{SWNIR} > 0	NHI_{SWIR} > 0 AND NHI_{SWNIR} > 0
Volgograd Oblast	599	238	61	234	57
North Dakota	478	33	8	30	5
Bayelsa	336	99	40	93	34
New South Wales	654	38	13	25	0
Basilicata	788	242	222	83	63
Persian Gulf	399	371	281	368	278

Fig. 6 shows changes in both frequency and intensity of gas flaring activity at each GF site, retrieved over a 6-year period (2015-2020). For the single offshore site analyzed here, the number of extremely hot pixels, which account for about the 52% of the 371 detections, is also reported (Fig. 6F).

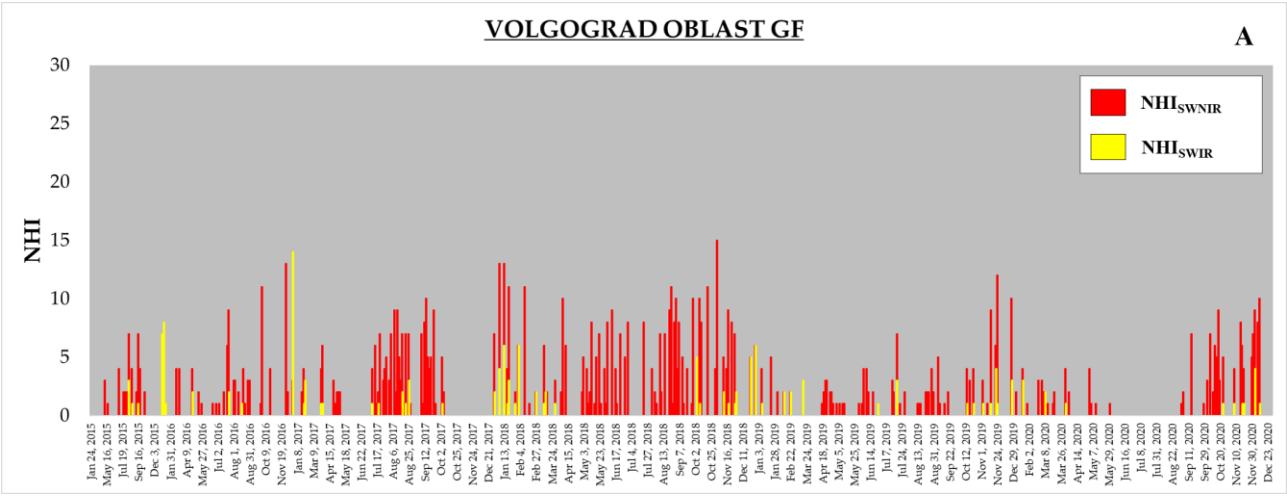

0196-2892 (c) 2021 IEEE. Personal use is permitted, but republication/redistribution requires IEEE permission. See http://www.ieee.org/publications_standards/publications/rights/index.html for more information.
Authorized licensed use limited to: CNR Area Ricerca Potenza. Downloaded on February 03,2022 at 16:38:15 UTC from IEEE Xplore. Restrictions apply.

This article has been accepted for publication in a future issue of this journal, but has not been fully edited. Content may change prior to final publication. Citation information: DOI 10.1109/TGRS.2022.3143167, IEEE Transactions on Geoscience and Remote Sensing

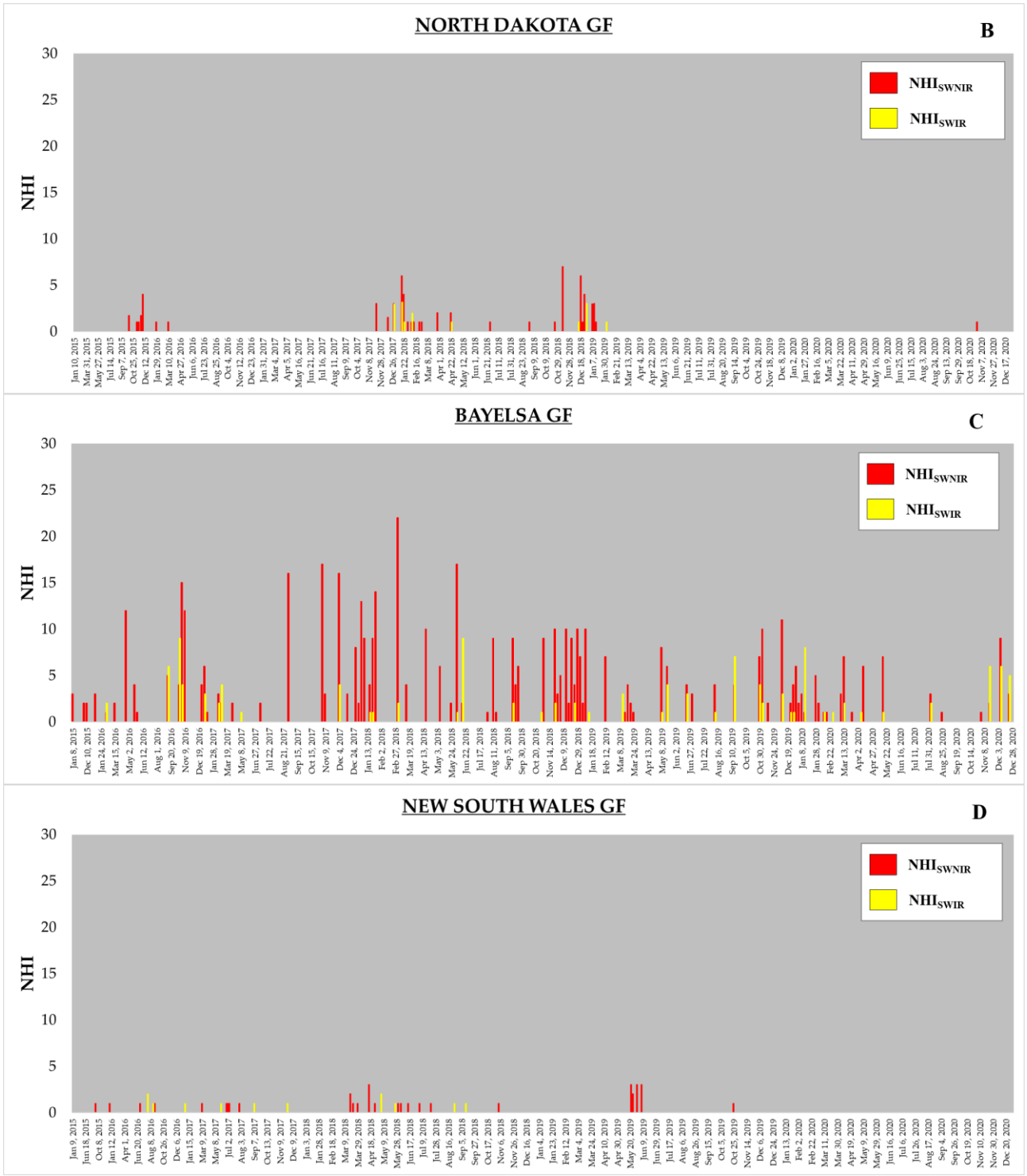

0196-2892 (c) 2021 IEEE. Personal use is permitted, but republication/redistribution requires IEEE permission. See http://www.ieee.org/publications_standards/publications/rights/index.html for more information.
Authorized licensed use limited to: CNR Area Ricerca Potenza. Downloaded on February 03,2022 at 16:38:15 UTC from IEEE Xplore. Restrictions apply.

This article has been accepted for publication in a future issue of this journal, but has not been fully edited. Content may change prior to final publication. Citation information: DOI 10.1109/TGRS.2022.3143167, IEEE Transactions on Geoscience and Remote Sensing

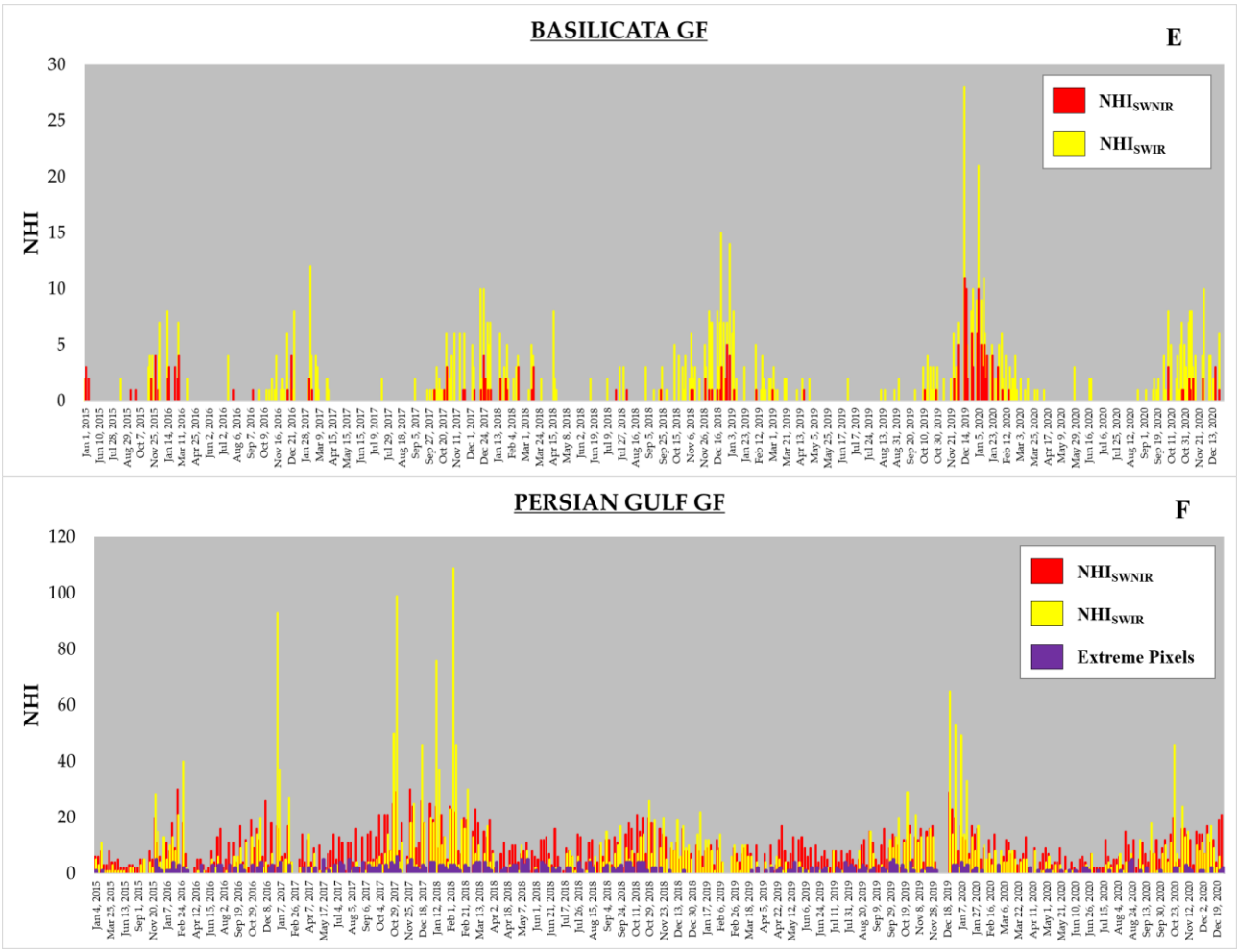

Fig 6. Temporal trend of daily hotspots flagged by NHI over A) Volgograd Oblast, B) North Dakota, C) Bayelsa, D) New South Wales, E) Basilicata, F) Persian Gulf gas flares.

The following considerations arise from the analysis of NHI detections detailed in Table 3 and shown in Fig. 6.

- A higher number (up to three times) of daily thermal anomalies was flagged over the Persian Gulf (Fig. 6F), in comparison with the other plants.
- A lower detection frequency characterized the onshore sites. The lowest values (i.e., less than 40 daily hotspots flagged by the algorithm) were recorded over North Dakota and New South Wales sites.
- The NHI_{SWNIR} index was the most effective in detecting thermal anomalies associated with the gas flaring activity (i.e., red pixels were prevalent), except from Basilicata site where the operational temperature is lower (section 2). This confirms that this index is the most sensitive to high intensity hotspots [18].
- Thermal anomalies flagged as "hot" by NHI included a single hot pixel (e.g., Australia) or a group of pixels located around the gas flaring source.

These findings indicate that NHI performed better in the offshore than onshore conditions, due to the different background, with a rate of success of 100% offshore (Persian Gulf) and up to 92% onshore (Nigerian site) (Fig. 7). Moreover, results indicate that some gas flare sites were not always operational during the investigated period (Fig. 6B and 6D). By the manual inspection of satellite imagery, we found that some thermal anomalies were affected by blurring effects (i.e., smearing of the emitted radiance across the adjacent pixels), occurring under specific sensor's field of view [39]. A weak flaring activity, the presence of clouds and aerosols [40], both natural (dust, volcanic ash, marine aerosols) and anthropogenic (traffic exhaust, biomass burning due to land clearance, road traffic) are the most common causes of missed flaring activity detections. Because satellite passive sensors are usually missing the tiny cirrus clouds [41], we assessed the impact of clouds on NHI sensitivity. Fig. 7 displays the percentage of cloudy scenes (retrieved from a visual inspection of satellite data) in reference to each analyzed flaring site and the NHI success rate.

A thorough and complete investigation of possible factors types may affect the missed detections will be the subject of future researches.

0196-2892 (c) 2021 IEEE. Personal use is permitted, but republication/redistribution requires IEEE permission. See http://www.ieee.org/publications_standards/publications/rights/index.html for more information.
Authorized licensed use limited to: CNR Area Ricerca Potenza. Downloaded on February 03,2022 at 16:38:15 UTC from IEEE Xplore. Restrictions apply.

This article has been accepted for publication in a future issue of this journal, but has not been fully edited. Content may change prior to final publication. Citation information: DOI 10.1109/TGRS.2022.3143167, IEEE Transactions on Geoscience and Remote Sensing

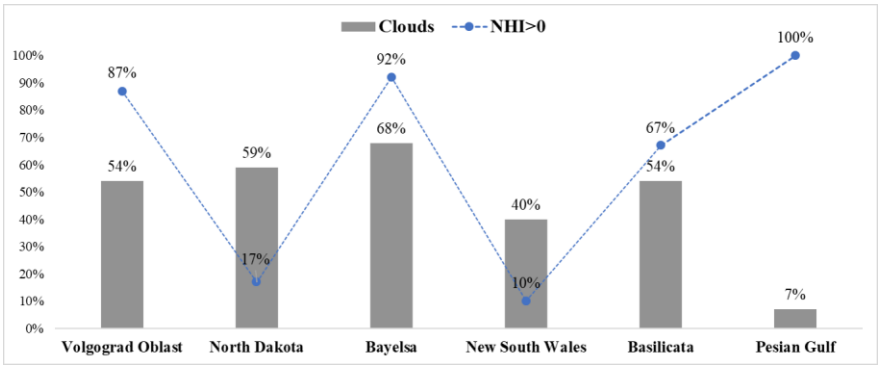

Fig 7. Percentage of cloudy scenes (grey histogram), and NHI success rate (blue line) determined by considering only the cloud-free imagery.

The histogram in Fig. 7 shows that clouds significantly affected the NHI detections, especially over the sites of Bayelsa and North Dakota. The lowest number of hotspots detected over the North Dakota and New South Wales sites may be addressed to the low-intensity and/or intermittent flares. This is confirmed by the comparison with the outputs of VNF algorithm, showing results in agreement with NHI. The other onshore sites were continuously operational in time, apart from Basilicata site showing a peculiar behavior (section 2).

The results shown and discussed so far were obtained without discriminating from S2-MSI from L8-OLI detections. To analyze the NHI algorithm behavior in a more accurate way over the selected flaring sites, we show in Fig. 8 the indices values plotted versus the L_{SWIR1}, L_{SWIR2} and L_{NIR} radiance differences, retrieved from daily hotspots in reference to the used sensors.

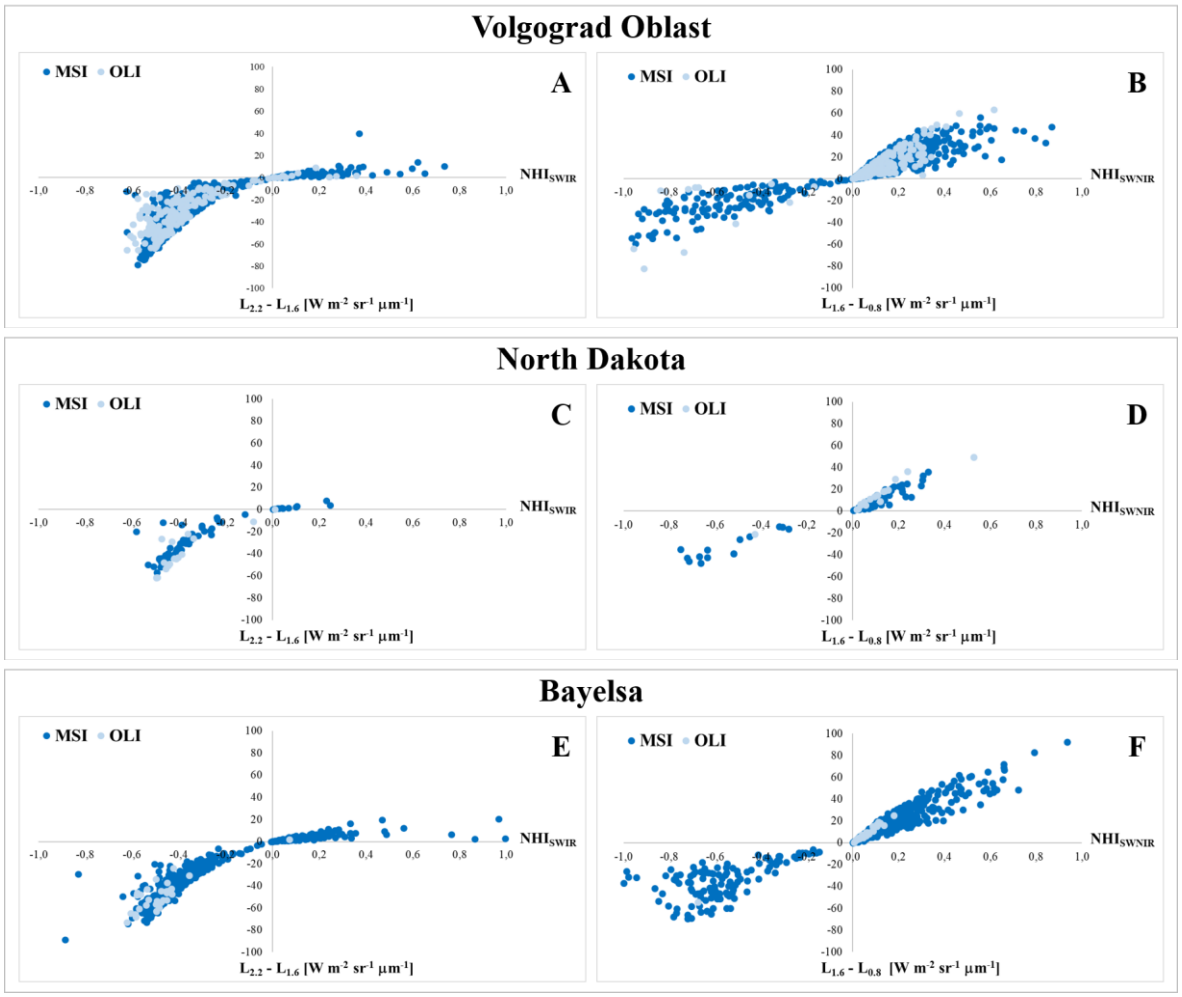

0196-2892 (c) 2021 IEEE. Personal use is permitted, but republication/redistribution requires IEEE permission. See http://www.ieee.org/publications_standards/publications/rights/index.html for more information.
Authorized licensed use limited to: CNR Area Ricerca Potenza. Downloaded on February 03,2022 at 16:38:15 UTC from IEEE Xplore. Restrictions apply.

This article has been accepted for publication in a future issue of this journal, but has not been fully edited. Content may change prior to final publication. Citation information: DOI 10.1109/TGRS.2022.3143167, IEEE Transactions on Geoscience and Remote Sensing

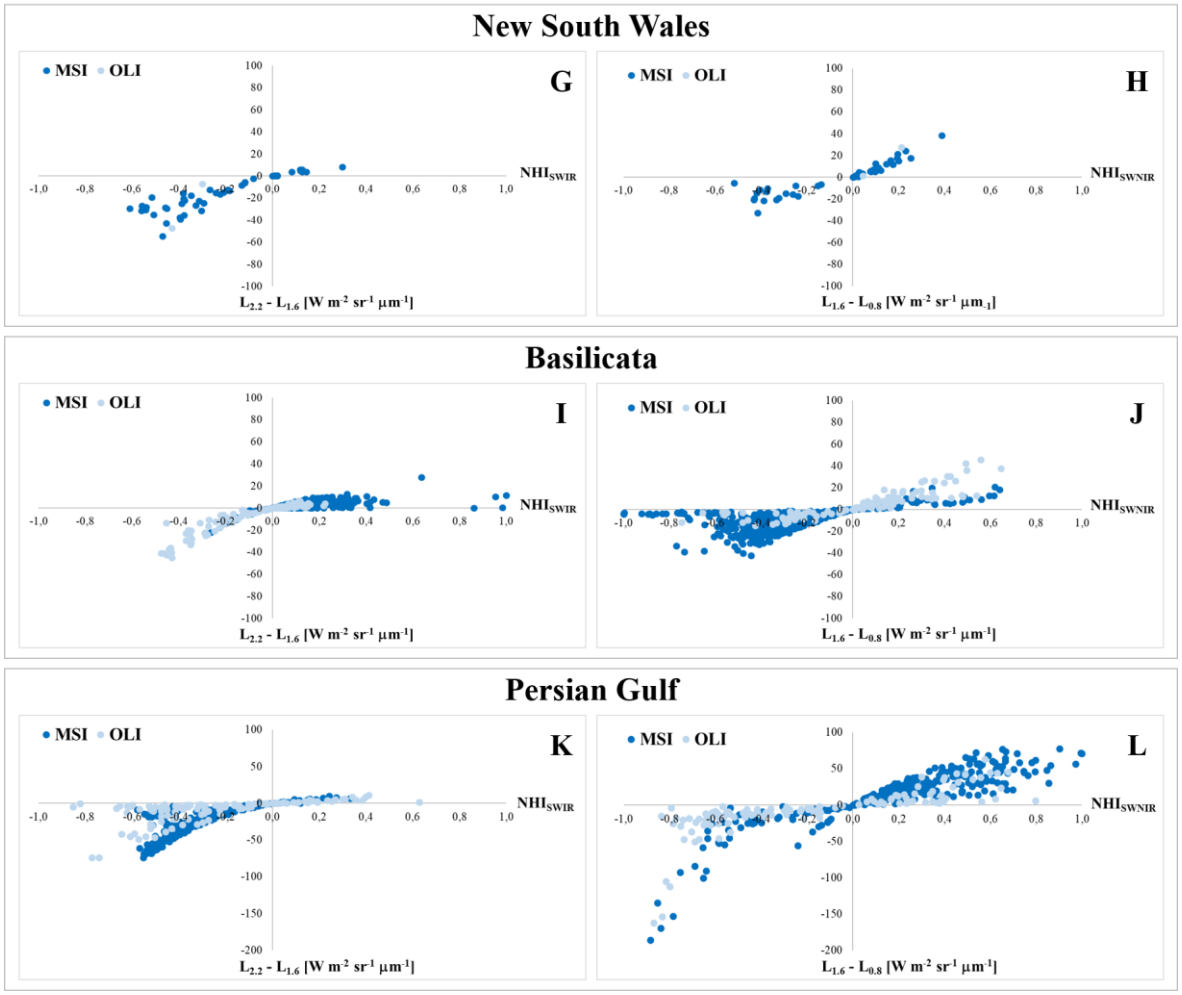

Fig 8. NHI_{SWIR} (on the left) and NHI_{SWNIR} (on the right) values versus radiances difference (MSI in dark blue, OLI in light blue) for A-B) Volgograd Oblast, C-D) North Dakota, E-F) Bayelsa, G-H) New South Wales, I-J) Basilicata, K-L) Persian Gulf.

Fig. 8 shows that the two NHI indices exhibited a similar behavior, regardless of used satellite data. For the NHI_{SWNIR} index, higher values of the radiance differences L_{SWIR1}-L_{NIR} (with the highest value of R=0.97 recorded at North Dakota), and a larger variation range than NHI_{SWIR} are observed. The lowest values belong to North Dakota (Fig. 8C-D) and New South Wales (Fig. 8G-H), representing intermittent flaring sites. The Basilicata site confirms its hybrid behavior, as shown and discussed above.

VI. Discussion

A. NHI implementation on coarse/medium spatial resolution data (VIIRS, SLSTR)

In the previous section, we have assessed the NHI potential in providing information about gas flaring activity in daylight conditions using S2-MSI and L8-OLI data. Results show that the algorithm is capable of detecting gas flaring thermal anomalies, in spite of some differences in between offshore and onshore conditions. On the other hand, since sensors such as VIIRS and SLSTR provide NIR and SWIR data suited to run the NHI algorithm (section 3), we verified if those data, at coarse spatial resolution, could be exploited to increase the frequency of observation of gas flare sites in daylight conditions. This is an important aspect, considering the significant impact of clouds on gas flaring identification especially in some geographic areas (e.g., Nigeria). Concerning the VIIRS data, we used both I- and M-bands to implement the algorithm. However, since VIIRS does not provide data at 375 m spatial resolution at the SWIR2 wavelengths, only the NHI_{SWNIR} index was computed. We selected two test sites, one onshore (i.e., Basilicata, Fig. 2F) and the other offshore (i.e., Persian Gulf, Fig. 2G), to perform this testing. We selected the Basilicata site to test the NHI algorithm on VIIRS and SLSTR data for the lowest temperatures and the more stringent operational conditions, which make the target the most challenging to investigate from space. On the contrary, the Persian Gulf site, which is the only located offshore, is representative of the most favorable observational conditions. Hence, we performed a cross-comparison analysis by selecting two SLSTR and VIIRS scenes temporally close (i.e., within a time interval of about 1 hour) to MSI and OLI observations (Table 4). In more detail, we analyzed data of December 24, 2017 for Basilicata site and of November 17, 2020 for the Persian Gulf.

TABLE IV

0196-2892 (c) 2021 IEEE. Personal use is permitted, but republication/redistribution requires IEEE permission. See http://www.ieee.org/publications_standards/publications/rights/index.html for more information.
Authorized licensed use limited to: CNR Area Ricerca Potenza. Downloaded on February 03,2022 at 16:38:15 UTC from IEEE Xplore. Restrictions apply.

This article has been accepted for publication in a future issue of this journal, but has not been fully edited. Content may change prior to final publication. Citation information: DOI 10.1109/TGRS.2022.3143167, IEEE Transactions on Geoscience and Remote Sensing

TEMPORAL AND SPATIAL CONSTRAINTS OF THE CROSS-COMPARISON ANALYSIS PERFORMED BY ANALYZING SATELLITE DATA OF DECEMBER 24, 2017 (ONSHORE) AND NOVEMBER 17, 2020 (OFFSHORE)

Satellite-sensor	Acquisition time (UTC) December 24, 2017	Acquisition time (UTC) November 17, 2020	Spatial resolution at nadir (m)
S2-MSI	09:54	07:01	20
L8-OLI	09:35	06:52	30
NPP (JPSS-1)-VIIRS	10:56	09:08	375
S3A-SLSTR	09:04	06:30	500
NPP-VIIRS	10:56	09:08	750

A spatial profile, of about 2500 m in length, crossing the Basilicata gas flares, was drawn (A-B transect in Fig. 9A) to assess the behavior of NHI indices and their capacity in detecting gas flaring activities when implemented on VIIRS and SLSTR data. In addition, we show in Fig. 9B the grid cell size characterizing the different sensors in reference to the target area (polygon in pink).

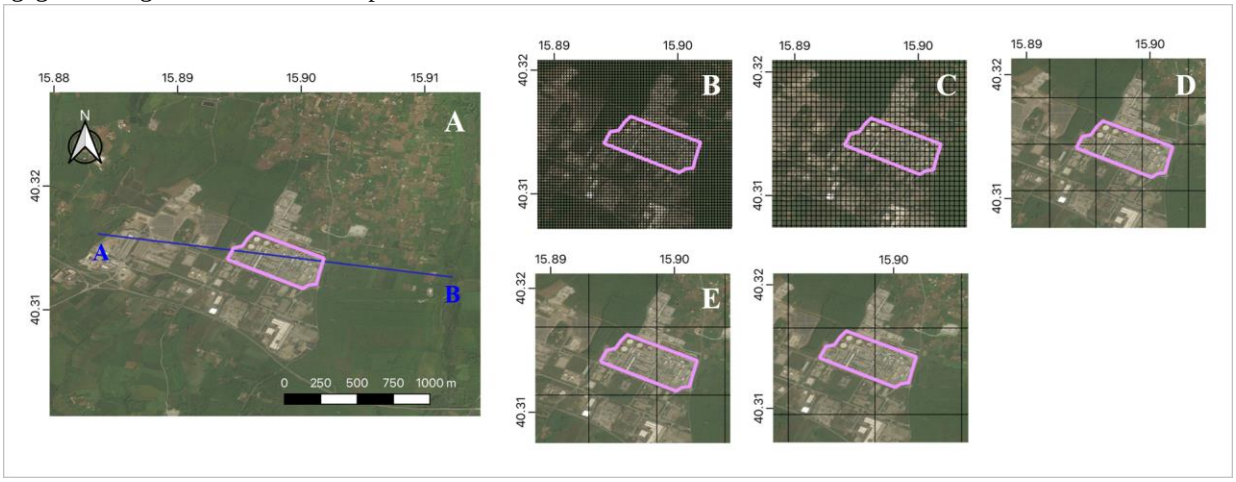

Fig 9. A) The Basilicata site (pink polygon) crossed by the spatial transect used in the analyses (blue line); B)-F) the Basilicata site within the 20-30-375-500-750 m grid. In background the Microsoft Bing map.

The infrared radiances measured along the A-B transect (Fig. 9A) are plotted in Fig. 10 (orange, yellow and green curves referring to NIR, SWIR1 and SWIR2, respectively).

0196-2892 (c) 2021 IEEE. Personal use is permitted, but republication/redistribution requires IEEE permission. See http://www.ieee.org/publications_standards/publications/rights/index.html for more information.
Authorized licensed use limited to: CNR Area Ricerca Potenza. Downloaded on February 03,2022 at 16:38:15 UTC from IEEE Xplore. Restrictions apply.

This article has been accepted for publication in a future issue of this journal, but has not been fully edited. Content may change prior to final publication. Citation information: DOI 10.1109/TGRS.2022.3143167, IEEE Transactions on Geoscience and Remote Sensing

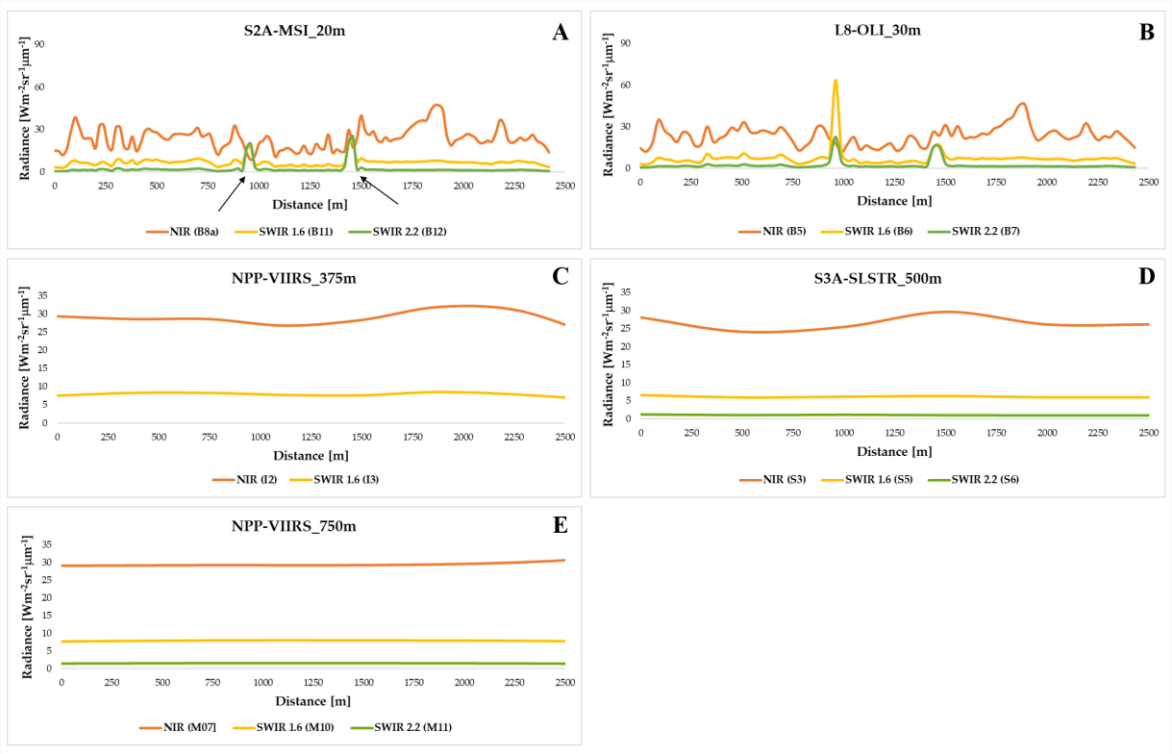

Fig 10. A) The NIR (orange line) and SWIR (yellow and green line at 1.6 and 2.2 μm) radiances retrieved along the A-B transect shown in Fig. 9A: A) S2A-MSI, B) L8-OLI, C) NPP-VIIRS (375 m), D) S3A-SLSTR, E) NPP-VIIRS (750 m). Black arrows indicate the position of the recovery sulphur (on the left side) and flares (on the right side) systems.

Fig. 10 shows the similar behavior of the signal regardless of used sensor, with the measured radiance increasing from high to low wavelengths (the highest radiance values were recorded in the NIR bands as expected in presence of background surfaces), fluctuating in a more significant way at the increasing spatial resolution. Indeed, the figure shows a significant increment of the S2-MSI and L8-OLI SWIR radiances only over gas flaring locations (950 m and 1450 m far from the "A" point of the transect), approaching the SWIR1 OLI channel saturation. In detail, we retrieved radiance values up to 64 W m^{-2} sr^{-1} μm^{-1} in the OLI SWIR1 band (22 W m^{-2} sr^{-1} μm^{-1} in the SWIR2 channel), and lower radiance values in the MSI SWIR channels, i.e., up to 21 (SWIR1) and 25 W m^{-2} sr^{-1} μm^{-1} (SWIR2). SWIR radiance values measured by VIIRS and SLSTR were comparable, although significantly lower than MSI and OLI. They ranged in between 6-8 (SWIR1) and 1.0-1.5 (SWIR2) W m^{-2} sr^{-1} μm^{-1}. Thus, high-temperature thermal anomalies associated with sub-pixel gas flares well detected by NHI using MSI/OLI data do not produce a significant increase of the SWIR radiance measured by VIIRS/SLSTR over land areas (Fig. 10 C-E).

As for the onshore gas flare, spatial plots along the A-B transect crossing the Persian Gulf platform (~2300 m in length) were obtained by analyzing data of November 17, 2020.

0196-2892 (c) 2021 IEEE. Personal use is permitted, but republication/redistribution requires IEEE permission. See http://www.ieee.org/publications_standards/publications/rights/index.html for more information.
Authorized licensed use limited to: CNR Area Ricerca Potenza. Downloaded on February 03,2022 at 16:38:15 UTC from IEEE Xplore. Restrictions apply.

This article has been accepted for publication in a future issue of this journal, but has not been fully edited. Content may change prior to final publication. Citation information: DOI 10.1109/TGRS.2022.3143167, IEEE Transactions on Geoscience and Remote Sensing

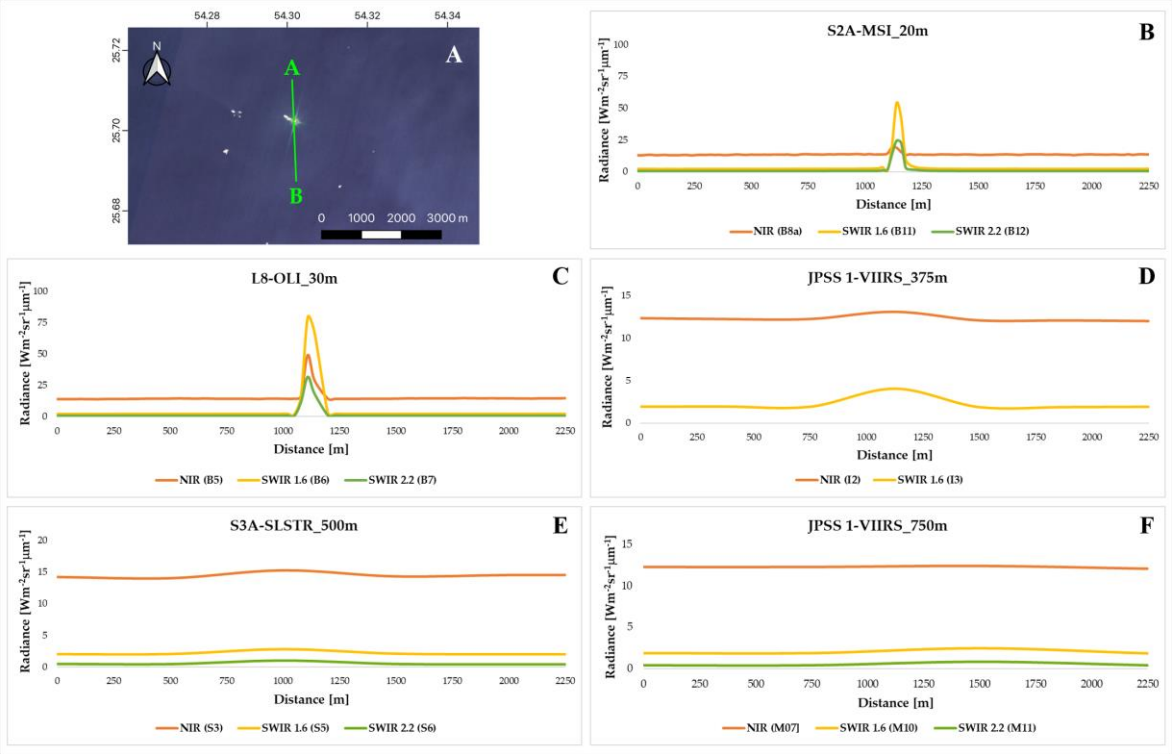

Fig. 11. As Fig. 10, for the offshore site; A) the false color RGB (B11, B12, B8a) composite of the S2A-MSI image of November 17, 2020 at 07:01 UTC in background.

Fig. 11 highlights the lower fluctuations of the NIR/SWIR radiance, measured along the aforementioned transect, in comparison with the onshore conditions. The presence of gas flare located at around 1.0 km far from the left edge of transect is marked by the MSI/OLI SWIR spatial profile. It is worth noting that a similar peak was recorded also in the NIR band. This spatial signature is highlighted in the offshore context by the almost total signal absorption by the water (and therefore, by the nil contribution in terms of radiance measured at the sensor, apart from the atmospheric component) in the VNIR spectral region. In this condition, even data at coarse spatial resolution may enable the hotspot identification. By looking at the plot of Fig. 10D-E, referring to images acquired at 375 m (VIIRS) and 500 m (SLSTR) spatial resolution respectively, a general increase of the measured radiance is evident (especially at 375 m) just in correspondence of the gas flares. In particular, an increase of SWIR2 radiance higher than 110% (average value among the three bands), when compared to the background, is measured at the flare pixel. The radiance increment was lower (i.e., around 35%) in the SWIR1 band, and much less significant in the NIR band (< 8%). Moreover, since the NIR radiance is higher than the SWIR1, which in turn is higher than SWIR2, the NHI indices remains negative. To better investigate this behavior, Fig. 12 shows the NHI profiles retrieved along the transects intersecting the onshore (Fig. 12 A,C) and offshore (Fig. 12B,D) gas flare sites. The NHI_{SWNIR} is shown on the top and NHI_{SWIR} on the bottom.

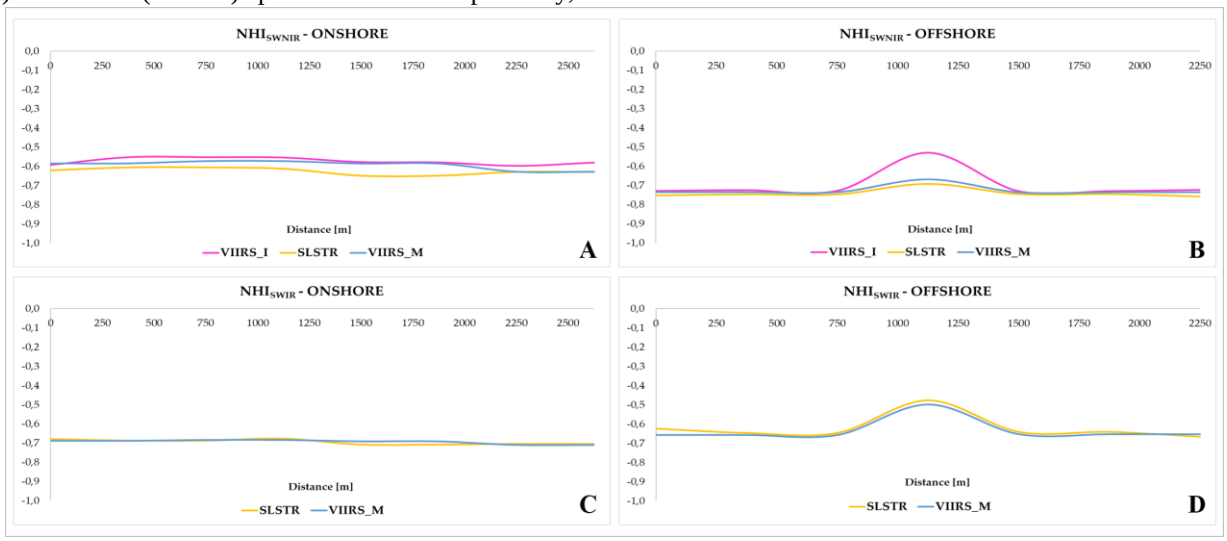

0196-2892 (c) 2021 IEEE. Personal use is permitted, but republication/redistribution requires IEEE permission. See http://www.ieee.org/publications_standards/publications/rights/index.html for more information.
Authorized licensed use limited to: CNR Area Ricerca Potenza. Downloaded on February 03,2022 at 16:38:15 UTC from IEEE Xplore. Restrictions apply.

This article has been accepted for publication in a future issue of this journal, but has not been fully edited. Content may change prior to final publication. Citation information: DOI 10.1109/TGRS.2022.3143167, IEEE Transactions on Geoscience and Remote Sensing

Fig. 12. Spatial profiles of NHI_{SWNIR} (on the top) and NHI_{SWIR} (on the bottom) values for the onshore (left side) and offshore (right side) gas flares along the corresponding transects (shown in Fig. 9A and 11A).

It can be noted as both normalized indices are negative regardless of gas flares location. On the other hand, while the two NHI indices did not show significant variations onshore (Fig. 12A-C), they increased offshore (up to -0.4, Fig. 12B-D). This behavior indicates that a threshold different from that used to detect thermal anomalies through MSI and OLI data could enable the identification of gas flaring activity in this specific condition. To corroborate this hypothesis, we computed the NHI indices over five cloud-free VIIRS images acquired in December 2020, analyzing the signal measured only in the M-bands. Results shown in Fig. 13 seem to confirm the above-mentioned speculation, marking the increase of both NHI indices over the Persian Gulf site (a major increment characterizes the NHI_{SWIR} index; see bottom panel).

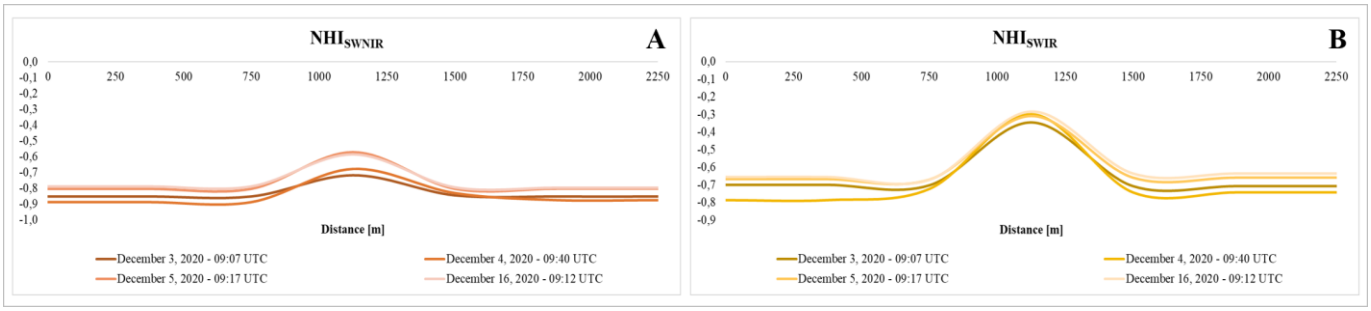

Fig. 13. A) NHI_{SWNIR} and B) NHI_{SWIR} values along the A-B profile crossing the Persian Gulf platform, shown in Fig. 11A.

B. *Future perspectives*

Up to now, a multi-sensor system, integrating daytime and nighttime observations over gas flare areas has not been designed, mainly because of issues affecting satellite observations at coarse spatial resolution acquired in daylight conditions. This paper demonstrates that a similar system could be developed by exploiting satellite observations at mid-high spatial resolution. In addition, results shown in this paper indicate that the NHI algorithm could be in principle used (with ad-hoc dynamic thresholds) to retrieve information about thermal anomalies also over maritime platforms using satellite data at coarse spatial resolution. An example of this potential system is shown in Fig. 14, where thermal anomalies flagged by NHI in daytime over the Basilicata site during 2017-2018 are depicted in yellow, together with hotspots detected in nighttime by VNF, marked in blue.

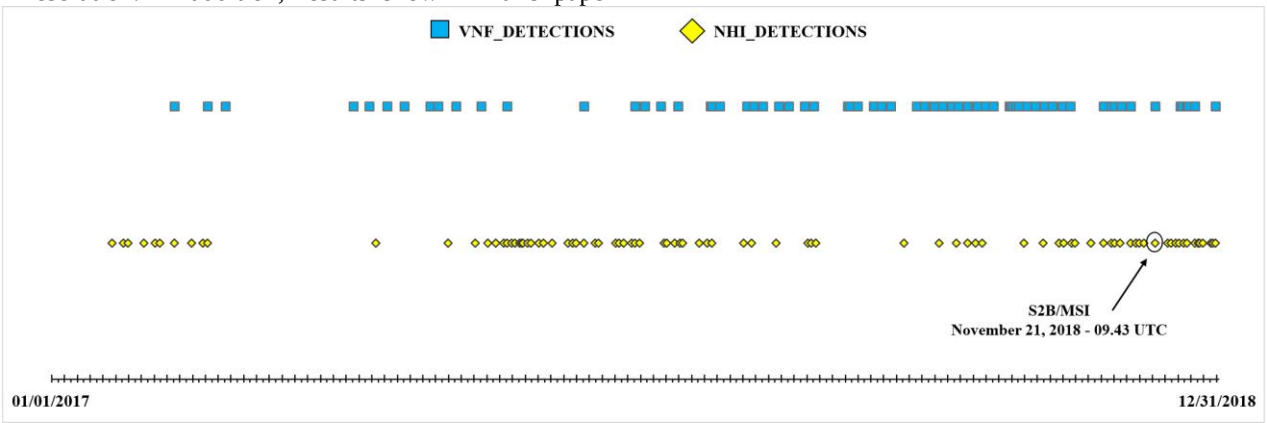

Fig. 14. Days with thermal anomalies detected in nighttime (VNF, blue squares) and daytime (NHI, yellow rhombus) over Basilicata site during 2017-2018. The black circle highlights an anomalous event occurred at the plant [42].

The time series of NHI and VNF detections exhibits the presence of some observational gaps, due to clouds, smoke, low thermal emissions and no-activity periods for each observing system (Fig. 14). By indicating with L the length of this temporal gap, the maximum value is equal to 79 and 104 days for the nighttime (VNF) and the daytime (NHI) system, respectively. Both data refer to the period April-July 2017, when activity at the Basilicata plant stopped [43]. The average temporal gap measured for the two platforms is quite similar (i.e., 11 against 8). If we consider the number of temporal windows without thermal anomaly detections of at least 20 days, we reduced it (as well as the L value) of about 30% by integrating daytime and nighttime observations, improving the hotspot tracking significantly. This integration is particularly for the Basilicata site, where anomalous events (in terms of amount of burned gas) occur due to the combustion operations and/or emergency gas flaring. These events are sporadic but relevant, because considered dangerous to health and safety by local citizens [22]. A satellite system performing continuous observations (in both daytime and nighttime) could represent a valuable source of information in this urbanized area. An example is shown in Fig. 14, where the black arrow indicates the thermal anomaly identified by NHI on 21 November at 10:15 UTC (11:15 LT), when the Italian National Hydrocarbons Authority (ENI), who manages the Basilicata

0196-2892 (c) 2021 IEEE. Personal use is permitted, but republication/redistribution requires IEEE permission. See http://www.ieee.org/publications_standards/publications/rights/index.html for more information.
Authorized licensed use limited to: CNR Area Ricerca Potenza. Downloaded on February 03,2022 at 16:38:15 UTC from IEEE Xplore. Restrictions apply.

This article has been accepted for publication in a future issue of this journal, but has not been fully edited. Content may change prior to final publication. Citation information: DOI 10.1109/TGRS.2022.3143167, IEEE Transactions on Geoscience and Remote Sensing

plant, reported the occurrence of an anomalous event at the Basilicata plant, missed by the nighttime VNF records, during the routine maintenance activities, lasting about 15 minutes [41].

These results emphasize the relevance of L8-OLI and S2-MSI observations, which complementing information from operational systems using satellite data at coarse spatial resolution acquired in nighttime, could enable a more continuous monitoring of gas flaring activity at different sites.

VII. Conclusion

In this work, we have assessed the potential of the NHI algorithm in detecting and monitoring thermal anomalies associated with gas flaring, through daytime Landsat-8 OLI and Sentinel-2 MSI data. The slightly different spectral, spatial and temporal characteristics of the two sensors do not affect the NHI performances, thus making their combined use a strength of the proposed method. Anyway, despite some limitations (e.g., lower sensitivity in specific onshore conditions, clouds/smoke), the operational NHI usage opens new and challenging scenarios regarding the daytime monitoring and characterization of gas flaring activity. Indeed, taking into account the recently launch of the Landsat 9 platform, which reduced to 8 days the temporal coverage of OLI observations [44], the NHI tool may build daytime maps of GF sites with an unprecedented frequency, also in areas (and/o in periods) where (when) clouds persistence might possibly represent a challenge.

This study also explored NHI capabilities when used on sensors at lower spatial resolution (i.e. VIIRS and SLSTR), further extending the possibility to observe and check these peculiar hot sources in daytime conditions.

A web-based application performing globally, capable of providing information about thermal anomalies with advantages of OLI and MSI data integration, in both onshore and offshore environment, is under development. This system could fill the observational gaps in the gas flaring analysis mainly associated with the use of nighttime satellite data. Besides, the tool under development could even provide estimates of GF fire radiative power as well as of volumes of emitted gas, complementing information from other satellite datasets (e.g., VIIRS).

Acknowledgment

The authors thank the members of the Earth Observation Group, Payne Institute for Public Policy, C. D. Elvidge and T. Sparks, for providing the VIIRS NightFire data for the investigated test sites.

References

[1] International Energy Agency (IEA), Putting gas flaring in the spotlight. Commentary, 9 December 2020, 2020. Available: https://www.iea.org/commentaries/putting-gas-flaring-in-the-spotlight.

[2] B. M. Conrad, M. R. Johnson. “Field Measurements of Black Carbon Yields from Gas Flaring”, Environmental Science & Technology, 51(3), 1893–1900, 2017. doi:10.1021/acs.est.6b03690.

[3] H. Semmari, A. Filali, S. Aberkane, R. Feidt, M. Feidt. “Flare Gas Waste Heat Recovery: Assessment of Organic Rankine Cycle for Electricity Production and Possible Coupling with Absorption Chiller”, Energies, 13(2265), 2020. doi: 10.3390/en13092265.

[4] The World Bank, Zero Routine Flaring by 2030. Available: https://www.worldbank.org/en/programs/zero-routine-flaring-by-2030.

[5] The World Bank - Global Gas Flaring Reduction Partnership (WB - GGFR), Global Gas Flaring Tracker Report. Available: https://thedocs.worldbank.org/en/doc/1f7221545bf1b7c89b850dd85cb409b0-0400072021/original/WB-GGFR-Report-Design-05a.pdf.

[6] FLUENTA. 2020 Flaring: A year in review. Available: https://www.fluenta.com/2020-flaring-a-year-in-review/.

[7] M. Franklin, K. Chau, L. J. Cushing, J. E. Johnston. “Characterizing Flaring from Unconventional Oil and Gas Operations in South Texas Using Satellite Observations”, Environmental Science & Technology, 53(4), 2220–2228, 2019. doi: 10.1021/acs.est.8b05355.

[8] J. E. Johnston, K. Chau, M. Franklin, L. Cushing. “Environmental Justice Dimensions of Oil and Gas Flaring in South Texas: Disproportionate Exposure among Hispanic communities”, Environmental Science & Technology, 54(10), 6289–6298, 2020. doi: 10.1021/acs.est.0c00410.

[9] M. Faruolo, A. Caseiro, T. Lacava, J. W. Kaiser. “Gas Flaring: A Review Focused on Its Analysis from Space (Review)”, IEEE Geoscience and Remote Sensing Magazine, 9(1), 258–281, 2021. doi:10.1109/MGRS.2020.3007232.

[10] C. D. Elvidge, M. Zhizhin, F.-C. Hsu, K. E. Baugh. “VIIRS Nightfire: Satellite pyrometry at night”, Remote Sens., 5(9), 4423–4449, 2013. doi: 10.3390/rs5094423.

[11] C. D. Elvidge, M. Zhizhin, K. E. Baugh, F.-C. Hsu, T. Ghosh. “Methods for global survey of natural gas flaring from Visible Infrared Imaging Radiometer Suite data”, Energies, 9(1), 2016. doi: 10.3390/en9010014.

[12] C. D. Elvidge, M. Zhizhin, K. Baugh, F. Hsu, T. Ghosh. “Extending Nighttime Combustion Source Detection Limits with Short Wavelength VIIRS Data”, Remote Sens., 11(4), 2019. doi: 10.3390/rs11040395.

[13] S. Casadio, O. Arino, A. Minchella. “Use of ATSR and SAR measurements for the monitoring and characterisation of night-time gas flaring from off-shore platforms: The North Sea test case”, Remote Sens. Environ., 123, 175–186, 2012. doi: 10.1016/j.rse.2012.03.021.

[14] O. C. D. Anejionu, G. A. Blackburn, J. D. Whyatt. “Satellite survey of gas flares: development and application of a Landsat based technique in the Niger Delta”, International Journal of Remote Sensing, 35(5), 1900–1925, 2014. doi: 10.1080/01431161.2013.879351

[15] S. Chowdhury, T. Shipman, D. Chao, C. D. Elvidge, M. Zhizhin, F.-C. Hsu, “Daytime gas flare detection using Landsat-8 multispectral data” in Proceedings of the IEEE International Geoscience Remote Sensing Symposium, Quebec City, Canada, 2014, pp. 258–261.

[16] Y. Liu, C. Hu, C. Sun, W. Zhan, S. Sun, B. Xu. “Assessment of offshore oil/gas platform status in the northern Gulf of Mexico using multi-source satellite time-series images”, Remote Sens. Environ., 208, 63–81, 2018. doi: 10.1016/j.rse.2018.02.003.

[17] N. Genzano, N. Pergola, F. Marchese. “A Google Earth Engine Tool to Investigate, Map and Monitor Volcanic Thermal Anomalies at Global Scale by Means of Mid-High Spatial Resolution Satellite Data”, Remote Sens., 12(3232), 1–22, 2020. doi: 10.3390/rs12193232.

[18] F. Marchese, N. Genzano, M. Neri, A. Falconieri, G. Mazzeo, N. Pergola. “A Multi-Channel Algorithm for Mapping Volcanic Thermal Anomalies by Means of Sentinel-2 MSI and Landsat-8 OLI Data”, Remote Sens., 11(2876), 1–25, 2019. doi: 10.3390/rs11232876.

[19] International Energy Agency (IEA), Flaring Emissions. Available: https://www.iea.org/reports/flaring-emissions.

0196-2892 (c) 2021 IEEE. Personal use is permitted, but republication/redistribution requires IEEE permission. See http://www.ieee.org/publications_standards/publications/rights/index.html for more information.
Authorized licensed use limited to: CNR Area Ricerca Potenza. Downloaded on February 03,2022 at 16:38:15 UTC from IEEE Xplore. Restrictions apply.

This article has been accepted for publication in a future issue of this journal, but has not been fully edited. Content may change prior to final publication. Citation information: DOI 10.1109/TGRS.2022.3143167, IEEE Transactions on Geoscience and Remote Sensing

[20] W. Lu, Y. Liu, J. Wang, W. Xu, W. Wu, Y. Liu, B. Zhao, H. Li, P. Li. "Global proliferation of offshore gas flaring areas", Journal of Maps, 16(2), 396–404, 2020. doi: 10.1080/17445647.2020.1762773.

[21] Reuters, World Bank says global gas flaring hit highest in over a decade in 2019. Available: https://www.reuters.com/article/us-worldbank-emissions/world-bank-says-global-gas-flaring-hit-highest-in-over-a-decade-in-2019-idUSKCN24M21Y.

[22] M. Faruolo, T. Lacava, N. Pergola, V. Tramutoli. "The VIIRS-Based RST-FLARE Configuration: The Val d'Agri Oil Center Gas Flaring Investigation in Between 2015–2019", Remote Sens., 12(819), 1–21, 2020. doi: 10.3390/rs12050819.

[23] M. Faruolo, I. Coviello, C. Filizzola, T. Lacava, N. Pergola, V. Tramutoli. "A satellite-based analysis of the Val d'Agri Oil Center (southern Italy) gas flaring emissions", Nat. Hazards Earth Syst. Sci., 14, 2783–2793, 2014. doi: 10.5194/nhess-14-2783-2014.

[24] S. Plank, F. Marchese, N. Genzano, M. Nolde, S. Martinis. "The short life of the volcanic island New Late'iki (Tonga) analyzed by multi-sensor remote sensing data", Scientific reports, 10(22293), 2020. doi: 10.1038/s41598-020-79261-7.

[25] G. Mazzeo, M. S. Ramsey, F. Marchese, N. Genzano, N. Pergola. "Implementation of the NHI (Normalized Hot Spot Indices) Algorithm on Infrared ASTER Data: Results and Future Perspectives", Sensors, 21(1538), 2021. https://doi.org/10.3390/s21041538.

[26] A. Sharma, J. Wang, E. M. Lennartson. "Intercomparison of MODIS and VIIRS fire products in Khanty-Mansiysk Russia: Implications for characterizing gas flaring from space", Atmosphere, 8(12), 1–19, 2017. doi: 10.3390/atmos8060095.

[27] D. Fisher, and M. J. Wooster. "Multi-decade global gas flaring change inventoried using the ATSR-1, ATSR-2, AATSR and SLSTR data records", Remote Sens. Environ., 232(111298), 2019. doi: 10.1016/j.rse.2019.111298.

[28] USGS, Landsat 8 Collection 1 (C1) Land Surface Reflectance Code (LaSRC) Product Guide. Available: https://prd-wret.s3.us-west-2.amazonaws.com/assets/palladium/production/atoms/files/LSDS-1368_L8_C1-LandSurfaceReflectanceCode-LASRC_ProductGuide-v3.pdf.

[29] T. R. Loveland, and J. L. Dwyer. "Landsat: Building a strong future", Remote Sens. Environ., 122, 22–29, 2012. https://doi.org/10.1016/j.rse.2011.09.022.

[30] ESA, Sentinel-2: ESA's Optical High-Resolution Mission for GMES Operational Services. Available: https://sentinel.esa.int/documents/247904/349490/S2_SP-1322_2.pdf.

[31] ESA, Sentinel Online. User Guides. Level-1C. Available: https://earth.esa.int/web/sentinel/user-guides/sentinel-2-msi/product-types/level-1c.

[32] ESA Copernicus. S2 MPC- L1C Data Quality. Available: https://sentinel.esa.int/documents/247904/685211/Sentinel-2_L1C_Data_Quality_Report.

[33] W. Schroeder, P. Olivia, L. Giglio, I. A. Czizar. "The New VIIRS 375 m active fire detection data product: Algorithm description and initial assessment", Remote Sens. Environ., 143, 85–96, 2014. http://dx.doi.org/10.1016/j.rse.2013.12.008.

[34] A. Caseiro, G. Rücker, J. Tiemann, D. Leimbach, E. Lorenz, O. Frauenberger, J. W. Kaiser. "Persistent Hot Spot Detection and Characterisation Using SLSTR", Remote Sens., 10(7), 2018. doi: 10.3390/rs10071118.

[35] N. Gorelick, M. Hancher, M. Dixon, S. Ilyushchenko, D. Thau, R. Moore. "Google Earth Engine: Planetary-scale geospatial analysis for everyone", Remote Sens. Environ., 202, 18–27, 2017. https://doi.org/10.1016/j.rse.2017.06.031.

[36] R. Morfitt, J. Barsi, R. Levy, B. Markham, E. Micijevic, L. Ong, P. Scaramuzza, K. Vanderwerff. "Landsat-8 Operational Land Imager (OLI) radiometric performance on-orbit", Remote Sens., 7, 2208–2237, 2015. https://doi.org/10.3390/rs70202208.

[37] ESA, Sentinel Online. Revisit and Coverage. Available: https://sentinels.copernicus.eu/web/sentinel/user-guides/sentinel-2-msi/revisit-coverage.

[38] W. Schroeder, P. Oliva, L. Giglio, B. Quayle, E. Lorenz, F. Morelli. "Active fire detection using Landsat-8/OLI data", Remote Sens. Environ., 185, 210–220, 2016. https://doi.org/10.1016/j.rse.2015.08.032.

[39] F. Massimetti, D. Coppola, M. Laiolo, S. Valade, C. Cigolini, M. Ripepe. "Volcanic Hot-Spot Detection Using SENTINEL-2: A Comparison with MODIS–MIROVA Thermal Data Series", Remote Sens., 12(5), 820, 2020. https://doi.org/10.3390/rs12050820.

[40] S. S. Kumar, J. Hult, J. Picotte, B. Peterson. "Potential Underestimation of Satellite Fire Radiative Power Retrievals over Gas Flares and Wildland Fires", Remote Sens., 12(238), 2020. https://doi.org/10.3390/rs12020238.

[41] T. M. McHardy *et al.*, "Advancing Maritime Transparent Cirrus Detection Using the Advanced Baseline Imager "Cirrus" Band," *Journal of Atmospheric and Oceanic Technology*, vol. 38, no. 6, pp. 1093-1110, 2021.

[42] ENI, Eni in Basilicata, News: Evento di visibilità della torcia del Centro Olio Val d'Agri. Available: https://www.eni.com/eni-basilicata/news/2018/2018-11-21-visibilita-torcia-centro-olio-valdagri.page. In Italian.

[43] ENI, Eni in Basilicata, News: Eni annuncia la chiusura del COVA. Available: https://www.eni.com/eni-basilicata/news/2017/2017-04-18-eni-annuncia-chiusura-cova.page. In Italian.

[44] USGS, Landsat Missions. Available: https://www.usgs.gov/core-science-systems/nli/landsat/landsat-9?qt-science_support_page_related_con=0#qt-science_support_page_related_con.

0196-2892 (c) 2021 IEEE. Personal use is permitted, but republication/redistribution requires IEEE permission. See http://www.ieee.org/publications_standards/publications/rights/index.html for more information.
Authorized licensed use limited to: CNR Area Ricerca Potenza. Downloaded on February 03,2022 at 16:38:15 UTC from IEEE Xplore. Restrictions apply.